ACSNANO

www.acsnano.org

ARTICLE

Hot-Carrier Generation in Plasmonic Nanoparticles: The Importance of Atomic Structure

Tuomas P. Rossi,* Paul Erhart,* and Mikael Kuisma*

Cite This: *ACS Nano* 2020, 14, 9963–9971

Read Online

ACCESS | Metrics & More | Article Recommendations | Supporting Information

ABSTRACT: **Metal nanoparticles are attractive for plasmon-enhanced generation of hot carriers, which may be harnessed in photochemical reactions. In this work, we analyze the coherent femtosecond dynamics of photon absorption, plasmon formation, and subsequent hot-carrier generation through plasmon dephasing using first-principles simulations. We predict the energetic and spatial hot-carrier distributions in small metal nanoparticles and show that the distribution of hot electrons is very sensitive to the local structure. Our results show that surface sites exhibit enhanced hot-electron generation in comparison to the bulk of the nanoparticle. Although the details of the distribution depend on particle size and shape, as a general trend, lower-coordinated surface sites such as corners, edges, and {100} facets exhibit a higher proportion of hot electrons than higher-coordinated surface sites such as {111} facets or the core sites. The present results thereby demonstrate how hot carriers could be tailored by careful design of atomic-scale structures in nanoscale systems.**

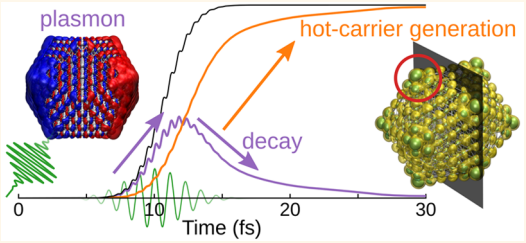

KEYWORDS: *localized surface plasmon, plasmon decay, plasmon dephasing, time-dependent density functional theory, hot electrons, hot carriers, atomic scale*

Plasmon-enhanced technologies enabled by metal nanoparticles (NPs) provide promising avenues for harvesting and converting sunlight to chemical energy[1] and driving photochemical reactions.[2] The underlying processes rely on the decay of plasmonic excitations and the subsequent generation of high-energy non-equilibrium electrons and holes.[3] These electrons and holes are often collectively referred to as hot carriers (HCs), but their distributions can vary substantially with time after excitation.[4,5] HCs generated by plasmon decay can, in principle, be transferred to a chemically attached acceptor such as a semiconductor or a molecule, a process that is potentially useful for technologies such as photovoltaics,[6] photodetection,[7,8] photon up-conversion,[9] and photocatalysis[2,10−13] and possibly relevant for NP growth processes.[14]

It can be challenging to develop comprehensive understanding of plasmon-generated hot carriers *via* purely experimental approaches both due to time constraints and the difficulty associated with disentangling different contributions.[15−17] In this context, complementary theoretical and computational approaches can provide highly valuable insight as they enable scrutinizing the relevant microscopic processes. The present theoretical understanding of plasmonic HC generation is mostly based on flat metal surfaces[18,19] or jellium NPs neglecting the underlying atomic structure.[4,5,20−26] Whereas atomic-scale effects in nanoplasmonics, in general, have been increasingly addressed in recent years,[27−32] atomic-scale modeling of plasmonic HC generation is only emerging.[33−35] In particular, detailed atomic-scale distributions of plasmon-generated HCs, to our knowledge, have not yet been scrutinized. In the context of photocatalysis detailed understanding of plasmonic HC generation at the atomic scale is, however, of paramount importance as chemical reactions take place at this size scale.

In this work, we analyze the effect of local atomic-scale structure on plasmonic HC generation and demonstrate that the distribution of HCs after plasmon decay is sensitive to the atomic-scale details. Using a series of NPs, we analyze quantitatively the spatial distribution of plasmon-generated HCs at the atomic scale with respect to surface orientation as well as for edge and corner sites. As the trends are consistent across NPs of different size and shape, the trends obtained here are expected to be transferable to more general nanoscale

Received: April 9, 2020
Accepted: July 20, 2020
Published: July 20, 2020

https://dx.doi.org/10.1021/acsnano.0c03004
ACS Nano 2020, 14, 9963–9971

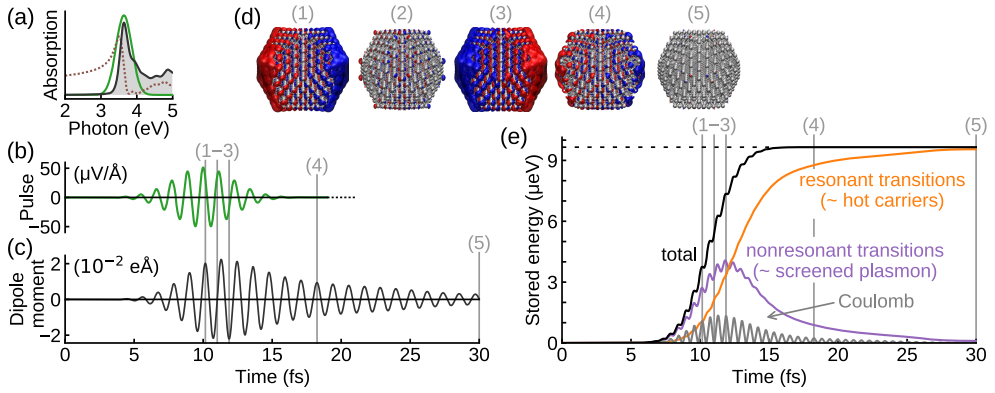

Figure 1. Real-time dynamics of a localized surface plasmon in a silver nanoparticle. (a) Photoabsorption spectrum of the Ag_{561} NP (shaded) and the intensity profile of an impacting electric field pulse (green). Photoabsorption is determined by the imaginary part of the polarizability, α, and the corresponding real part, $\mathrm{Re}[\alpha]$, is shown as a dotted line. (b) Electric field pulse impacting the plasmon resonance of the NP. (c) Time-dependent dipole moment response of the NP. (d) Electron density oscillations in the NP at selected time instances (red and blue isosurfaces denote density increase and decrease, respectively). (e) Time evolution of the energy stored in the excited electronic system. The total energy (black) is divided into the energy of nonresonant electron−hole transition contributions constituting screened plasmon excitation (purple) and that of resonant transition contributions constituting mainly hot carriers (orange). A part of the plasmon energy is in the form of Coulomb energy (gray).

structures. For this study, we have developed a fully atomistic, parameter-free, and generally applicable description of plasmonic HC generation based on Kohn−Sham (KS) density functional theory (DFT)[36,37] and time-dependent density functional theory (TDDFT).[38]

RESULTS AND DISCUSSION

Real-Time Dynamics of Localized Surface Plasmon. To introduce our approach for modeling plasmonic HC generation, we start with a comprehensive characterization of plasmon formation and subsequent dephasing. We consider an icosahedral Ag_{561} silver NP as an example system with a clear plasmon resonance in the photoabsorption spectrum (Figure 1a).[39] The ground-state electronic structure of the NP is calculated with DFT using the Gritsenko−van Leeuwen−van Lenthe−Baerends−solid-correlation (GLLB-sc) exchange-correlation (XC) potential[40,41] for an improved d-band description.[28,42] The time-dependent response is then calculated with TDDFT using either the random-phase approximation (RPA) or the adiabatic GLLB-sc[28] (see Methods for details).

To excite the localized surface plasmon resonance (LSPR) in the NP, we use a monochromatic ultrafast Gaussian light pulse

$$\mathcal{E}(t) = \mathcal{E}_0 \cos(\omega_0(t - t_0))\exp(-(t - t_0)^2/\tau_0^2) \quad (1)$$

that induces real-time dynamics of electrons in the system. The pulse frequency $\omega_0 = 3.6$ eV is tuned to the plasmon resonance, the pulse duration is determined by $\tau_0 = 3$ fs, and the pulse is centered at $t_0 = 10$ fs (Figure 1b). The pulse strength is weak, $\mathcal{E}_0 = 51$ μV/Å, putting the response in the linear-response regime. In the frequency space, the pulse is wide enough to cover the whole plasmon resonance (Figure 1a).

The interaction between electrons and light is described in the dipole approximation, within which the light pulse creates a time-dependent external potential, $v_{\mathrm{pulse}}(t) = z\mathcal{E}(t)$, that causes the time evolution of the KS states $|\psi_n(t)\rangle$ and excitation of the LSPR. The light pulse induces a strong dipole-moment response [Figure 1c(1−3)]. The corresponding electron density oscillations [Figure 1d(1−3)] are composed of a surface-to-surface component associated with delocalized valence electrons near the Fermi energy and atom-localized contributions that correspond to screening due to virtual excitations from the d-band.[39] As time proceeds to $t \approx 17$ fs, the excited electrons start to lose their collective plasmonic motion *via* a dephasing process commonly referred to as Landau damping.[43] As the plasmon dephases, the dipole moment decays [Figure 1c(4,5)] corresponding to vanishing surface-to-surface density oscillation [Figure 1d(4,5)].[33] Whereas the density oscillations and dipole moment response gives an illustrative picture of the plasmon formation and decay, they seem not to provide a tractable way for scrutinizing HC contributions to the response. To this end, we consider the time-dependent energy contributions of different KS transitions.

Time-Dependent Energy Contributions. As the pulse is tuned to the LSPR, the electronic system absorbs energy from the incident light and remains in an excited state after the pulse has vanished. To analyze the distribution of this energy, we first consider the total time-dependent energy of the system given by

$$E_{\mathrm{tot}}(t) = E_{\mathrm{tot}}^{(0)} + \Delta E(t) + E_{\mathrm{pulse}}(t) \quad (2)$$

where $E_{\mathrm{tot}}^{(0)}$ is the ground-state energy, $\Delta E(t)$ is the time-dependent energy stored in the excited state (Figure 1e, black line), and $E_{\mathrm{pulse}}(t) = -\mu(t)\mathcal{E}(t)$ is the potential energy of the system under the external electric field.

The incident light pulse pumps energy into the system; that is, it does work on the system as $\Delta\dot{E}(t) = \delta\dot{\mu}(t)\mathcal{E}(t)$, where dots indicate time derivatives and $\delta\mu(t) = \mu(t) - \mu^{(0)}$ is the induced dipole moment. Thus, the total accumulated electronic energy can be written as

$$\Delta E(t) = \int_0^t \delta\dot{\mu}(\tau)\mathcal{E}(\tau)\mathrm{d}\tau \quad (3)$$

The electronic energy increases through absorption in a stepwise manner following the pulse intensity (Figure 1e, $t \approx 5$...15 fs). After the pulse has ended ($t \gtrsim 15$ fs), the absorbed energy remains in the system and the total energy has attained a new constant value given by the photoabsorption cross section (Figure 1a and eq 11 in Methods).

Although the total energy remains constant, the electronic energy does not stay equally distributed among the electron−hole transitions $i \rightarrow a$ excited by the light pulse. To quantify this

https://dx.doi.org/10.1021/acsnano.0c03004
ACS Nano 2020, 14, 9963−9971

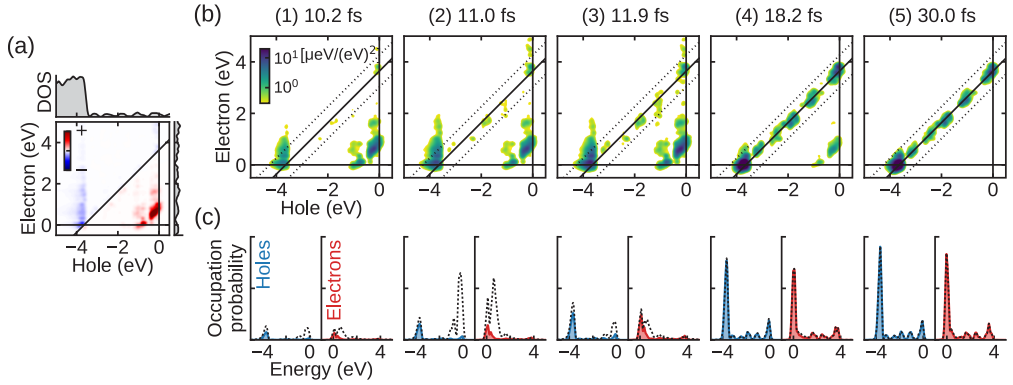

Figure 2. Electron−hole transition contributions to plasmon formation and decay. (a) Electron−hole contributions to the photoabsorption at the resonance energy visualized as a transition contribution map (TCM). Density of states is also shown along the energy axes. (b) Electron−hole contributions to the time-dependent electronic energy visualized as TCM on a logarithmic color scale. The solid diagonal line corresponds to the transition energies matching with the pulse frequency ω_0 and the dotted diagonal lines are drawn at $\omega_0 \pm 2\sigma$ to indicate the pulse width $\sigma = \sqrt{2}/\tau_0$, defining the boundaries for resonant and nonresonant transitions for Figure 1e. (c) Occupation probabilities of hole and electron states. Solid blue and red lines denote state occupations from resonant transitions, and dashed lines denote occupations from all transitions (resonant and nonresonant). The figure columns (1−5) show panels (b) and (c) for the time instances labeled in Figure 1. The color scale and axis limits are the same in all of the columns.

effect, we consider the decomposition of the energy in electron−hole transition contributions. This decomposition is based on the linear response of the KS density matrix, $\delta\rho_{ia}(t)$, expressed in the basis of the eigenstates $(\epsilon_n, \psi_n^{(0)})$ of the ground-state Hamiltonian. The electron−hole decomposition of energy is (see Supplementary Note S1 for derivation)

$$\Delta E(t) = \sum_{ia}^{f_i > f_a} \omega_{ia} P_{ia}(t) + E_{ia}^{C}(t) \tag{4}$$

where the sum is restricted by ground-state occupation numbers f_n so that the indices i and a correspond to the created hole and electron states, respectively. Here, $\omega_{ia} = \epsilon_a - \epsilon_i$ is the electron−hole transition energy (the KS eigenvalue difference), $P_{ia}(t)$ is the transition probability defined as

$$P_{ia}(t) = \left| \frac{\delta\rho_{ia}(t)}{\sqrt{f_i - f_a}} \right|^2 \tag{5}$$

and $E_{ia}^{C}(t)$ is the Coulomb energy as obtained from the Hartree−XC kernel (defined in Supplementary Note S1).

Plasmon formation and dephasing can be scrutinized by considering the energy stored in the electronic system in terms of the electron−hole transition energy, ω_{ia}, with respect to the pulse frequency ω_0 (Supplementary Figure S1). The plasmon is formed by constructive coupling of low-energy transitions [$\omega_{ia} \lesssim 2$ eV; see Figure 2a and time instances (1−3) in Figure 2b].[39,43,44] Simultaneously, high-energy virtual d-electron transitions ($\omega_{ia} \gtrsim 4$ eV) screen the plasmonic density oscillation, decreasing the total induced field. The energy stored in the screening is similar to the energy stored in the polarization of a dielectric in general; that is, as the total field strength decreases, energy is instead stored in the polarization of the d-electron states as in $\omega_{ia}P_{ia}(t)$ in eq 4. The nonresonant low- and high-energy transitions carry most of the energy during plasmon excitation (Figure 1e, purple line). As the plasmon dephases, the absorbed energy is redistributed to electron−hole transitions that are resonant with the pulse [Figure 1e, orange line; corresponding to the diagonal in the transition contribution maps in Figure 2b; see time instances (4,5)]. After dephasing, the energy remains almost exclusively stored in these transitions constituting the plasmon-generated HCs. The transitions comprising the plasmon are active in photoabsorption (Figure 2a), and hot holes and electrons are generated through plasmon decay, instead of the HC transitions absorbing the light directly (shown in detail in Supplementary Figure S2).

At longer time scales, the electronic system would dissipate the absorbed energy to the environment *via* radiation, atomic motion, or other processes, but such decay pathways are not included within the description used here. Thus, in the present picture, there appears no significant dynamics in Ag_{561} at time scales beyond $t \gtrsim 30$ fs after the fast dephasing of the LSPR through Landau damping, which takes place due to the presence of multiple excitation eigenstates forming the broadened plasmon peak in the photoabsorption spectrum[43] (Supplementary Figure S3). However, the dynamics can be very different in small clusters with a discrete excitation spectrum. In contrast to a single broad plasmon peak in Ag_{561}, for example, in the Ag_{55} cluster, individual electron−hole transitions couple strongly to the plasmon,[39] a process that is referred to as plasmon fragmentation.[45,46] Correspondingly, the time-domain response exhibits Rabi oscillations and energy transfer back from the resonant transitions to the plasmon[33,47] (Supplementary Figure S4).

As the coupling of transitions *via* Coulomb interaction is recognized as an essential characteristic of plasmonic excitations,[39,43,44,48] it is instructive to consider the Coulomb energy, $E_C(t) = \sum_{ia} E_{ia}^{C}(t)$. This energy exhibits strong oscillations (Figure 1e, gray line) analogous to the dipole moment (Figure 1c) as only the electron density oscillation contributes to the Coulomb energy. At the maxima of the surface-to-surface density oscillation [time instances (1) and (3) in Figure 1d,e], the Coulomb contribution is a significant part of the plasmon energy, but at the minima between [*e.g.*, time instance (2)], the Coulomb energy is vanishing as the electronic energy is stored in the electron current flowing through the particle (Supplementary Figure S5).

Temporal Evolution of Hot-Carrier Distributions. Having established a real-time picture of plasmon formation and decay, we are in the position to analyze the distributions of

https://dx.doi.org/10.1021/acsnano.0c03004
ACS Nano 2020, 14, 9963−9971

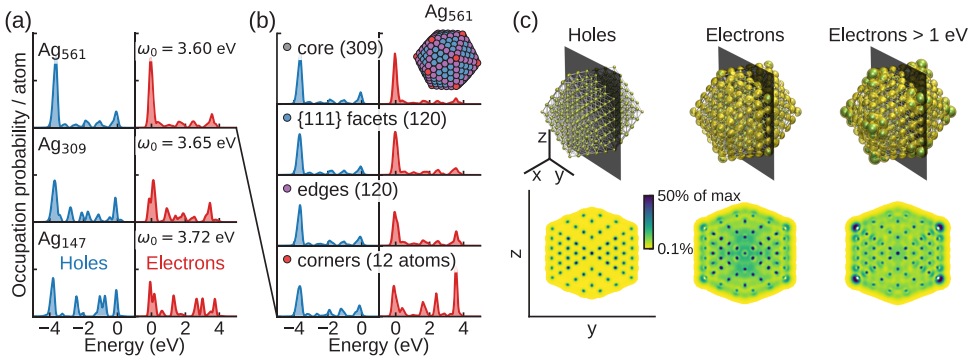

Figure 3. Hot-carrier distributions after plasmon decay. (a) Occupation probabilities of hole and electron states in icosahedral silver NPs of 147−561 atoms. (b) Occupation probabilities at different atomic sites of Ag_{561}. All the panels use the same axis limits (normalized by the number of atoms). (c) Spatial density profiles of all induced holes and electrons and induced electrons with energy of more than 1 eV in Ag_{561}. Plots show isosurfaces corresponding to 10 and 20% of maximum value, and slices are taken through the center of the NP.

electrons and holes during the process. The probabilities for creating a hole in an initially occupied state i or an electron in an initially unoccupied state a are given directly by the transition probability of eq 5 as

$$P_i^{\mathrm{h}}(t) = \sum_{a}^{f_i > f_a} P_{ia}(t) \text{ and } P_a^{\mathrm{e}}(t) = \sum_{i}^{f_i > f_a} P_{ia}(t) \tag{6}$$

respectively. P_i^{h} and P_a^{e} determine exactly the diagonal elements of the second-order response of the density matrix (Supplementary Note S1); in other words, they correspond to the increase of the occupation of the initially unoccupied state a and the decrease of the occupation of the initially occupied state i.

The occupation probabilities given by eq 6 show strong oscillations during the time evolution [Figure 2c(1−3), dashed lines]. These oscillations are explained by the oscillation of the Coulomb energy. As the Coulomb energy contribution is carried mainly by nonresonant transitions (Supplementary Figure S6), the occupation probabilities of the electron and hole states contributing to these nonresonant transitions oscillate analogously to the Coulomb energy. The oscillations are especially visible in the occupations of electron and hole states that form the plasmon,[35] that is, the states near the Fermi energy, often referred to as Drude carriers.[49] The oscillatory population and depopulation of these states indicate that they would not likely be individually separable while they are a part of the plasmon as the Coulomb interaction is an essential part of the excitation itself.[50]

The contributions of the resonant transitions to the Coulomb energy are relatively small (Supplementary Figure S6), and the occupations of the corresponding electron and hole states grow steadily as the plasmon decays (Figure 2c, solid lines). At the end of the dynamic evolution studied here [Figure 2c(5)], electrons and holes are still coupled in the form of electron−hole transitions, and the distributions at t = 30 fs can be considered as the initial nonthermal HC distributions. After their generation, these carriers would separate and interact *via* electron−electron and electron−phonon scattering processes[3,5,19,51] that are not captured in the present description. The slight asymmetry between the hole and electron distributions is caused by a nonzero width of the pulse in the frequency space (Figure 1a).

Energetic and Atomic-Scale Spatial Distributions of Hot Carriers. We now analyze the distribution of plasmon-generated hot carriers and the impact of local atomic-scale structure. We start by considering the series of icosahedral silver NPs Ag_{147}, Ag_{309}, and Ag_{561}, the photoabsorption properties of which we have described in detail in previous work[28,39] (see Supplementary Figure S7 for photoabsorption spectra and densities of states). The light pulse is tuned to the plasmon resonance of the NPs, and the initial HC distributions are analyzed after the plasmon has dephased at a time t = 30 fs. The HC distributions show a pronounced dependence on NP size (Figure 3a) and local structure (Figure 3b,c) as discussed in the following.

As particle size increases, the HC distributions are increasingly dominated by interband d-electron transitions[26] (hole ∼ −4 eV → electron ∼0 eV) converging toward the distributions obtained for flat surfaces.[18,19] In contrast to extended systems, geometry confinement effects are significant for plasmonic HC generation in nanoscale systems.[52] Due to the broken crystal symmetry, additional "intraband" transitions are available for plasmonic HC generation in NPs, which results in the population of higher-energy electron and hole states (Figure 3a; electron states of >0.5 eV, hole states of >−3.5 eV). The relative contribution of these sp-states is most pronounced in the smallest NPs[26] (Ag_{147}, Ag_{309}), but they are non-negligible also in Ag_{561}. Similar size-dependent trends are also present in silver NPs of other shapes, whereas the detailed relative contributions of different transitions vary (Supplementary Figure S8).

The calculated probability distributions of plasmon-generated electrons and holes (see Methods) exhibit strong spatial variance (shown for the icosahedral Ag_{561} NP in Figure 3b,c): Holes are localized at atomic sites throughout the particle, which is expected as the majority of holes originates from the atom-localized d-states. As a result, their energy distribution is very similar for core and surface sites. Hot electrons, on the other hand, are more delocalized and reside to larger extent in the surface region. The surface contribution is even more pronounced for higher-energy hot electrons (>1 eV electrons in Figure 3c). The probability density of these hot electrons is strongly enhanced especially at low-coordinated edge and corner sites compared to sites in the core and on flat surfaces (Figure 3b). The energetic distributions of plasmon-generated holes and electrons are not necessarily symmetric when projected onto a particular site (Figure 3b and Supplementary Figure S8). This asymmetry is especially pronounced for the corner site in Ag_{561}, which reflects the fact that the hot-electron density at corner sites originates likely from throughout the particle due to the uniformity of the hole density.

https://dx.doi.org/10.1021/acsnano.0c03004
ACS Nano 2020, 14, 9963−9971

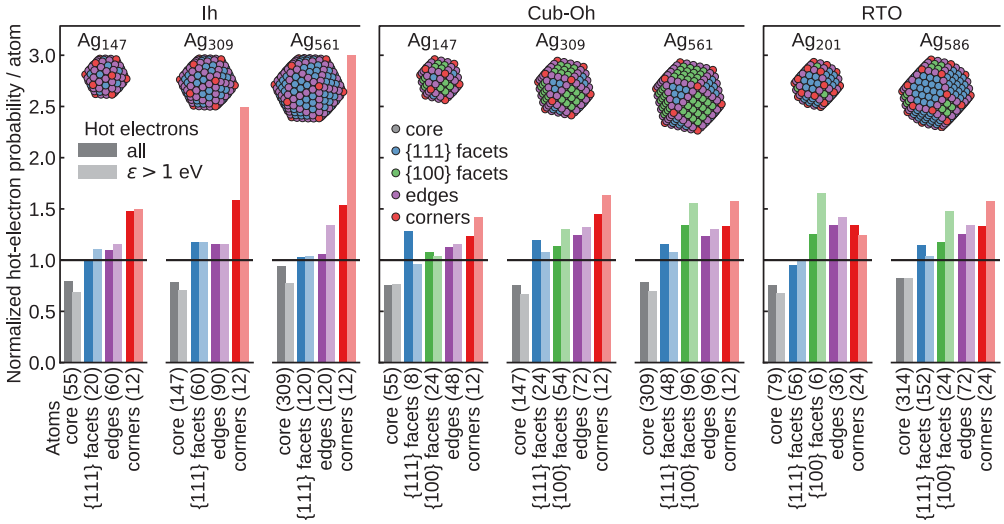

Figure 4. Atomic-scale distributions of hot electrons in silver nanoparticles. Spatial distribution of hot electrons generated on different atomic sites in icosahedral (Ih), cuboctahedral (Cub-Oh), and regularly truncated octahedral (RTO) NPs. Sites with lower coordination exhibit a higher proportion of hot electrons than core sites. A spatially uniform distribution corresponds to a normalized probability of unity. The insets show the atomic structures with the different atomic sites colored.

A more quantitative view is obtained by considering the total per-atom occupation probability of hot electrons at a particular atomic site in comparison to the total per-atom occupation probability throughout the system (Figure 4). These data suggest that in the icosahedral Ag_{561} NP, hot electrons with more than 1 eV are almost three times more likely to be found in the vicinity of a corner site than a uniform spatial distribution would correspond to. We emphasize that these are per-atom considerations; that is, as the 12 corner atoms constitute only around 2% of the atoms in the particle, it is expected that about 6% of the electrons with more than 1 eV would be generated in the vicinity of the corner atoms. Overall, hot electrons with more than 1 eV constitute 30−60% of all hot electrons depending on system (Supplementary Figure S8). The absolute total number of HCs generated depends on the light energy that is absorbed, which is in turn determined by the photoabsorption cross section and light intensity.

Similarly to icosahedral shapes, hot electrons in the cuboctahedral and regularly truncated octahedral NPs are more likely to be generated at a surface site than at a core site (Figure 4). The preference for surface sites is even more pronounced for hot electrons with more than 1 eV. The corner sites of the cuboctahedral and regularly truncated octahedral NPs, however, do not show as enhanced distribution of hot electrons as those sites of the icosahedral Ag_{561} particle. This further underlines the sensitivity of HC generation to atomic-scale details and the exact electronic structure of the NP and site(s) in question.

As a general trend, lower-coordinated sites seems to exhibit an enhancement of hot electrons compared to higher-coordinated sites. This trend is observed for corner and edge sites, but the data for cuboctahedral and regularly truncated octahedral NPs suggest also that more hot electrons are generated on the lower-coordinated {100} surface than on the {111} surface. In contrast to strong spatial variation of hot electrons, plasmon-generated holes do not show strong spatial dependence in the considered NPs (Supplementary Figure S9).

For practical utilization, HCs need to be transferred to the environment. The HC distributions obtained in the present work can be considered as the initial nonthermal HC distributions before any electron−electron scattering[19,51] has taken place. Thus, these HC distributions could serve as an initial condition for subsequent dynamics[3,5] that is not included in the present approach. In general, HC transfer to environment can occur *indirectly* (*i.e.*, carriers are first produced in the metal and subsequently transferred to the acceptor) or *directly* (*i.e.*, plasmon dephasing leads directly to the injection of HCs in empty acceptor, or occupied donor, states).[2,53−62] However, both experiments[63−65] and calculations[51,52,65,66] indicate that HCs generated in the metal can quickly relax through electron−electron scattering, which renders the indirect pathway inefficient. The direct-transfer process, on the other hand, presents an opportunity to obtain more efficient plasmonic HC devices.[54,56,62] The prevalence of hot electrons on lower-coordinated surface sites described in the present work seems favorable for their utility through the direct transfer processes. It is, however, crucial to also consider the hybridization of the surface electronic states with acceptor states, where the latter can originate, for example, from an adsorbed molecule[67] or a semiconductor.[68,69] To maximize the efficiency for direct excitation transfer, the emitting and receiving states should be energetically aligned and spatially overlapping. In addition, hot-electron generation can be affected by the dielectric environment, for example, by red-shifting the plasmon resonance so that d-band electrons are not excited. The framework presented here enables analysis and quantification of these aspects at the atomic scale with material specificity and without resorting to empirical parameters.

CONCLUSIONS

In conclusion, we presented a comprehensive first-principles account of the real-time dynamics of plasmon formation and dephasing into HCs and analyzed quantitatively the impact of atomic-scale structure on the HC generation. Our results on silver NPs indicate that lower-coordinated surface sites exhibit a larger proportion of *hot electrons*, especially those with higher energy, than the bulk of the nanoparticle or higher-coordinated surface sites. In contrast, the distribution of *hot holes* is relatively homogeneous within each considered NP. These features can be traced to the electronic structure as hole and electron states

https://dx.doi.org/10.1021/acsnano.0c03004
ACS Nano 2020, 14, 9963−9971

exhibit localized d- and delocalized sp-type character, respectively. We would therefore expect the present insight to be qualitatively transferable to other late transition metals that exhibit similar electronic structure. The observed trends are present in NPs of different shapes and sizes with varying prevalence. We therefore envision that the obtained atomic-scale insights could be applicable to nanoscale structures in general. First-principles predictions of plasmonic HC generation, as presented here, can thereby facilitate tuning and optimizing photocatalytic systems down to the atomic scale, for example, by enabling identification of promising surface-acceptor combinations.

METHODS

Computational Details. The ground-state electronic structures were calculated with KS-DFT[36,37] using the GLLB-sc exchange-correlation potential.[40,41] The time-domain responses were calculated with TDDFT[38] starting from the ground state. The dynamical response was described with RPA for the data in Figures 1 and 2 and in Supplementary Figures S1−S6, whereas all the other data were calculated with the adiabatic GLLB-sc.[28] The two response kernels yield very similar results (Supplementary Figure S10), but the GLLB-sc potential is not suitable for obtaining the total energies.

All of the calculations were carried out with the open-source GPAW code package[70] using localized basis sets[71] and the real-time propagation TDDFT implementation.[28] We used 11-electron projector-augmented wave[72] setups for Ag, treating the remaining electrons as a frozen core. We used an extended "p-valence" basis set that includes diffuse 5p functions, which are important for describing plasmon resonances.[73] The basis set is similar to the ones used in refs 28 and 39.

The photoabsorption spectra were calculated using the δ-kick technique,[74] yielding linear impulse response. The photoabsorption of icosahedral particles is isotropic, and the electric field was aligned along the x direction. The resulting HCs do not exhibit a strong variation between different sites (Figure 3c). For the time propagation, we used a time step of 10 as and total propagation time of at least 30 fs. The spectra were broadened using Gaussian damping with σ = 0.07 eV corresponding to a full width at half-maximum of 0.16 eV. The real-time response to a pulse was calculated as a postprocessing step through convolution as described below in detail. In the convolution Fourier transforms or time-domain response, there is no artificial damping.

A grid spacing parameter of h = 0.3 Å was chosen to represent densities and potentials, and the nanoparticles were surrounded by a vacuum region of at least 6 Å. The Hartree potential was evaluated with a Poisson solver using the monopole and dipole corrections for the potential. Fermi−Dirac smearing was applied to the occupation numbers to facilitate convergence. The KS electron−hole basis included electron−hole pairs with occupation number difference $f_i - f_a \geq 10^{-3}$.

Before the response calculations, all geometries were relaxed using the BFGS optimizer in the open-source ASE package.[75] The relaxation calculations used the Perdew−Burke−Ernzerhof (PBE)[76] functional, double-ζ polarized (dzp) basis sets, and h = 0.2 Å.

Pulse Response from Convolution. The photoabsorption spectrum can be efficiently calculated from real-time propagation using the δ-kick perturbation[74] as in the linear-response regime all the frequencies are independent of each other. We utilize this property in the present work for calculating the linear response of the density matrix to the Gaussian pulse of eq 1 as a postprocessing step. First, the time propagation is carried out for perturbation $v_{\mathrm{kick}}(t) = zK_0\delta(t)$, yielding the impulse response of the system and the corresponding time-dependent density matrix $\delta\rho_{ia}^{\mathrm{kick}}(t)$. Then, in the linear-response regime, the response to the pulse of eq 1 is obtained as a convolution

$$\delta\rho_{ia}(t) = \frac{1}{K_0}\int_0^\infty \delta\rho_{ia}^{\mathrm{kick}}(\tau)\mathcal{E}(t-\tau)\mathrm{d}\tau \tag{7}$$

which can be very efficiently calculated in frequency space by employing the convolution theorem and inverse Fourier transform

$$\delta\rho_{ia}(t) = \frac{1}{2\pi K_0}\int_{-\infty}^\infty \delta\rho_{ia}^{\mathrm{kick}}(\omega)\mathcal{E}(\omega)\mathrm{e}^{-i\omega t}\mathrm{d}\omega \tag{8}$$

where $\delta\rho_{ia}^{\mathrm{kick}}(\omega)$ and $\mathcal{E}(\omega)$ are Fourier transforms of the respective time-domain quantities. Here, $\delta\rho_{ia}^{\mathrm{kick}}(\omega)$ can be efficiently calculated from the impulse response by using the computational framework developed in ref 39. The time derivatives required for calculating the energy (Supplementary Note S4) are obtained similarly as

$$\delta\dot{\rho}_{ia}(t) = -\frac{i}{2\pi K_0}\int_{-\infty}^\infty \omega\delta\rho_{ia}^{\mathrm{kick}}(\omega)\mathcal{E}(\omega)\mathrm{e}^{-i\omega t}\mathrm{d}\omega \tag{9}$$

$$\delta\ddot{\rho}_{ia}(t) = -\frac{1}{2\pi K_0}\int_{-\infty}^\infty \omega^2\delta\rho_{ia}^{\mathrm{kick}}(\omega)\mathcal{E}(\omega)\mathrm{e}^{-i\omega t}\mathrm{d}\omega \tag{10}$$

In practice, $\mathcal{E}(\omega)$ is nonvanishing only on a finite frequency interval (see Figure 1a), which narrows the integration limits.

It is emphasized that the time-dependent density matrix, $\delta\rho_{ia}(t)$, is a complex quantity in time domain, so in practical calculations, it is convenient to carry out Fourier transform for the real $\mathrm{Re}\delta\rho_{ia}(t)$ and imaginary $\mathrm{Im}\delta\rho_{ia}(t)$ parts separately to utilize the properties of Fourier transform of real quantities.

We also note in passing that the impulse response $\delta\rho_{ia}^{\mathrm{kick}}(\omega)$ can be equivalently calculated from the Casida linear-response frequency-space formalism.[39,77] Hence, the linear real-time response to any pulse can also be calculated from the Casida solutions by using the convolution of eq 8.

Total Absorbed Energy. By invoking Fourier transform, the total absorbed energy after the pulse has vanished is obtained as

$$\int_0^\infty \delta\dot{\mu}(t)\mathcal{E}(t)\mathrm{d}t = \frac{1}{2}\int_0^\infty S(\omega)|\mathcal{E}(\omega)|^2\mathrm{d}\omega \tag{11}$$

where $S(\omega) = \frac{2\omega}{\pi}\mathrm{Im}[\alpha(\omega)]$ is the dipole strength function, which equals the photoabsorption cross section safe for a constant multiplier.

Hot-Carrier Distributions. The hot-electron energy distributions corresponding to the state occupation probabilities P_a^{e} of eq 6 are obtained as (time dependence is not explicitly marked)

$$P_{\mathrm{e}}(\epsilon) = \sum_a P_a^{\mathrm{e}}\delta(\epsilon-\epsilon_a) = \frac{1}{2}\sum_{ia}^{f_i>f_a}(q_{ia}^2+p_{ia}^2)\delta(\epsilon-\epsilon_a) \tag{12}$$

where

$$q_{ia}(t) = 2\mathrm{Re}\delta\rho_{ia}(t)/\sqrt{2(f_i-f_a)}$$

and

$$p_{ia}(t) = -2\mathrm{Im}\,\delta\rho_{ia}(t)/\sqrt{2(f_i-f_a)}$$

that is, they correspond to the real and imaginary parts of $\delta\rho_{ia}$ (see Supplementary Note S2 for details). For visualization purposes, Gaussian smoothing (convolution) is applied with respect to the ϵ axis.

The spatial probability density of hot electrons is given by the full electron−electron part of the second-order density matrix as (see Supplementary Note S1 and note that only the real part contributes due to the hermiticity of the density matrix)

$$P_{\mathrm{e}}(\boldsymbol{r}) = \frac{1}{2}\sum_{iaa'}^{\substack{f_i>f_a\\ f_a=f_{a'}}}(q_{ia}q_{ia'}+p_{ia}p_{ia'})\psi_a^{(0)}(\boldsymbol{r})\psi_{a'}^{(0)}(\boldsymbol{r}) \tag{13}$$

The diagonal and degenerate states dominate the spatial density contributions, which allows us to define a spatio-energetic distribution

$$P_{\mathrm{e}}(\epsilon,\boldsymbol{r}) = \frac{1}{2}\sum_{iaa'}^{\substack{f_i>f_a\\ \epsilon_a=\epsilon_{a'}}}(q_{ia}q_{ia'}+p_{ia}p_{ia'})\psi_a^{(0)}(\boldsymbol{r})\psi_{a'}^{(0)}(\boldsymbol{r})\delta(\epsilon-\epsilon_a) \tag{14}$$

https://dx.doi.org/10.1021/acsnano.0c03004
ACS Nano 2020, 14, 9963−9971

which is used to calculate the spatial density of hot electrons with more than 1 eV as $P_e^{>1eV}(\boldsymbol{r}) = \int_{1eV}^{\infty} P_e(\epsilon, \boldsymbol{r})d\epsilon$, and the energy distribution of hot electrons in a spatial volume V as $P_e^V(\epsilon) = \int_V P_e(\epsilon, \boldsymbol{r})d\boldsymbol{r}$. The distribution at a specific atomic site (*e.g.*, corner atoms) is obtained by integration over the Voronoi cell associated with the site.

The spatial and energetic distributions of hot holes are calculated analogously to the electrons.

Software Used. The GPAW package[70,78] with linear combination of atomic orbitals (LCAO) mode[71] was used for DFT calculations. The real-time propagation LCAO-TDDFT implementation in GPAW[28] was used for the TDDFT calculations. Density-matrix-based analysis tools in frequency space[39] and in real time (present work) were used for analysis. The ASE library[75] was used for constructing atomic structures and geometry relaxation. The NumPy[79] and Matplotlib[80] Python packages and the VMD software[81,82] were used for processing and plotting data.

ASSOCIATED CONTENT

Supporting Information

The Supporting Information is available free of charge at https://pubs.acs.org/doi/10.1021/acsnano.0c03004.

Figures S1−S10 displaying supporting data, notes S1−S4 deriving equations, and supporting reference (PDF)

AUTHOR INFORMATION

Corresponding Authors

Tuomas P. Rossi − *Department of Physics, Chalmers University of Technology, SE-412 96 Gothenburg, Sweden;* orcid.org/0000-0002-8713-4559; Email: tuomas.rossi@chalmers.se

Paul Erhart − *Department of Physics, Chalmers University of Technology, SE-412 96 Gothenburg, Sweden;* orcid.org/0000-0002-2516-6061; Email: erhart@chalmers.se

Mikael Kuisma − *Department of Chemistry, Nanoscience Center, University of Jyväskylä, FI-40014 Jyväskylä, Finland;* orcid.org/0000-0001-8323-3405; Email: mikael.j.kuisma@jyu.fi

Complete contact information is available at: https://pubs.acs.org/10.1021/acsnano.0c03004

Notes

The authors declare no competing financial interest.

Scripts, input and data files are also available on Zenodo (https://doi.org/10.5281/zenodo.3927527).

ACKNOWLEDGMENTS

We acknowledge financial support from the Knut and Alice Wallenberg Foundation (2014.0226, 2015.0055), the Swedish Research Council (2015-04153), and the Swedish Foundation for Strategic Research (RMA15-0052). T.P.R. acknowledges support from the European Union's Horizon 2020 research and innovation programme under the Marie Skłodowska-Curie Grant Agreement No. 838996 and also thanks the Adlerbert Research Foundation and the Wilhelm and Martina Lundgren Foundation for support. M.K. acknowledges funding from Academy of Finland under Grant No. 295602. We acknowledge generous computational resources provided by the Swedish National Infrastructure for Computing (SNIC) at PDC (Stockholm), NSC (Linköping), and C3SE (Gothenburg) as well as by the CSC−IT Center for Science (Finland).

REFERENCES

(1) Aslam, U.; Rao, V. G.; Chavez, S.; Linic, S. Catalytic Conversion of Solar to Chemical Energy on Plasmonic Metal Nanostructures. *Nat. Catal.* **2018**, *1*, 656.

(2) Linic, S.; Aslam, U.; Boerigter, C.; Morabito, M. Photochemical Transformations on Plasmonic Metal Nanoparticles. *Nat. Mater.* **2015**, *14*, 567.

(3) Brongersma, M. L.; Halas, N. J.; Nordlander, P. Plasmon-Induced Hot Carrier Science and Technology. *Nat. Nanotechnol.* **2015**, *10*, 25.

(4) Saavedra, J. R. M.; Asenjo-Garcia, A.; García de Abajo, F. J. Hot-Electron Dynamics and Thermalization in Small Metallic Nanoparticles. *ACS Photonics* **2016**, *3*, 1637.

(5) Liu, J. G.; Zhang, H.; Link, S.; Nordlander, P. Relaxation of Plasmon-Induced Hot Carriers. *ACS Photonics* **2018**, *5*, 2584.

(6) Atwater, H. A.; Polman, A. Plasmonics for Improved Photovoltaic Devices. *Nat. Mater.* **2010**, *9*, 205.

(7) Knight, M. W.; Sobhani, H.; Nordlander, P.; Halas, N. J. Photodetection with Active Optical Antennas. *Science* **2011**, *332*, 702.

(8) Chalabi, H.; Schoen, D.; Brongersma, M. L. Hot-Electron Photodetection with a Plasmonic Nanostripe Antenna. *Nano Lett.* **2014**, *14*, 1374.

(9) Naik, G. V.; Welch, A. J.; Briggs, J. A.; Solomon, M. L.; Dionne, J. A. Hot-Carrier-Mediated Photon Upconversion in Metal-Decorated Quantum Wells. *Nano Lett.* **2017**, *17*, 4583.

(10) Mukherjee, S.; Libisch, F.; Large, N.; Neumann, O.; Brown, L. V.; Cheng, J.; Lassiter, J. B.; Carter, E. A.; Nordlander, P.; Halas, N. J. Hot Electrons Do the Impossible: Plasmon-Induced Dissociation of H_2 on Au. *Nano Lett.* **2013**, *13*, 240.

(11) Mubeen, S.; Lee, J.; Singh, N.; Krämer, S.; Stucky, G. D.; Moskovits, M. An Autonomous Photosynthetic Device in which All Charge Carriers Derive from Surface Plasmons. *Nat. Nanotechnol.* **2013**, *8*, 247.

(12) Kale, M. J.; Avanesian, T.; Christopher, P. Direct Photocatalysis by Plasmonic Nanostructures. *ACS Catal.* **2014**, *4*, 116.

(13) Swearer, D. F.; Zhao, H.; Zhou, L.; Zhang, C.; Robatjazi, H.; Martirez, J. M. P.; Krauter, C. M.; Yazdi, S.; McClain, M. J.; Ringe, E.; Carter, E. A.; Nordlander, P.; Halas, N. J. Heterometallic Antenna-Reactor Complexes for Photocatalysis. *Proc. Natl. Acad. Sci. U. S. A.* **2016**, *113*, 8916.

(14) Zhai, Y.; DuChene, J. S.; Wang, Y.-C.; Qiu, J.; Johnston-Peck, A. C.; You, B.; Guo, W.; DiCiaccio, B.; Qian, K.; Zhao, E. W.; Ooi, F.; Hu, D.; Su, D.; Stach, E. A.; Zhu, Z.; Wei, W. D. Polyvinylpyrrolidone-Induced Anisotropic Growth of Gold Nanoprisms in Plasmon-Driven Synthesis. *Nat. Mater.* **2016**, *15*, 889.

(15) Zhou, L.; Swearer, D. F.; Zhang, C.; Robatjazi, H.; Zhao, H.; Henderson, L.; Dong, L.; Christopher, P.; Carter, E. A.; Nordlander, P.; Halas, N. J. Quantifying Hot Carrier and Thermal Contributions in Plasmonic Photocatalysis. *Science* **2018**, *362*, 69.

(16) Sivan, Y.; Baraban, J.; Un, I. W.; Dubi, Y. Comment on "Quantifying Hot Carrier and Thermal Contributions in Plasmonic Photocatalysis. *Science* **2019**, *364*, No. eaaw9367.

(17) Dubi, Y.; Sivan, Y. Hot" Electrons in Metallic Nanostructures—Non-Thermal Carriers or Heating? *Light: Sci. Appl.* **2019**, *8*, 89.

(18) Sundararaman, R.; Narang, P.; Jermyn, A. S.; Goddard, W. A.; Atwater, H. A. Theoretical Predictions for Hot-Carrier Generation from Surface Plasmon Decay. *Nat. Commun.* **2014**, *5*, 5788.

(19) Bernardi, M.; Mustafa, J.; Neaton, J. B.; Louie, S. G. Theory and Computation of Hot Carriers Generated by Surface Plasmon Polaritons in Noble Metals. *Nat. Commun.* **2015**, *6*, 7044.

(20) Manjavacas, A.; Liu, J. G.; Kulkarni, V.; Nordlander, P. Plasmon-Induced Hot Carriers in Metallic Nanoparticles. *ACS Nano* **2014**, *8*, 7630.

(21) Besteiro, L. V.; Govorov, A. O. Amplified Generation of Hot Electrons and Quantum Surface Effects in Nanoparticle Dimers with Plasmonic Hot Spots. *J. Phys. Chem. C* **2016**, *120*, 19329.

(22) Yan, L.; Wang, F.; Meng, S. Quantum Mode Selectivity of Plasmon-Induced Water Splitting on Gold Nanoparticles. *ACS Nano* **2016**, *10*, 5452.

(23) Dal Forno, S.; Ranno, L.; Lischner, J. Material, Size, and Environment Dependence of Plasmon-Induced Hot Carriers in Metallic Nanoparticles. *J. Phys. Chem. C* **2018**, *122*, 8517.
(24) Ranno, L.; Dal Forno, S.; Lischner, J. Computational Design of Bimetallic Core-Shell Nanoparticles for Hot-Carrier Photocatalysis. *npj. Comput. Mater.* **2018**, *4*, 31.
(25) Román Castellanos, L.; Hess, O.; Lischner, J. Single Plasmon Hot Carrier Generation in Metallic Nanoparticles. *Commun. Phys.* **2019**, *2*, 47.
(26) Román Castellanos, L.; Kahk, J. M.; Hess, O.; Lischner, J. Generation of Plasmonic Hot Carriers from D-Bands in Metallic Nanoparticles. *J. Chem. Phys.* **2020**, *152*, 104111.
(27) Zhang, P.; Feist, J.; Rubio, A.; García-González, P.; García-Vidal, F. J. *Ab Initio* Nanoplasmonics: The Impact of Atomic Structure. *Phys. Rev. B: Condens. Matter Mater. Phys.* **2014**, *90*, 161407.
(28) Kuisma, M.; Sakko, A.; Rossi, T. P.; Larsen, A. H.; Enkovaara, J.; Lehtovaara, L.; Rantala, T. T. Localized Surface Plasmon Resonance in Silver Nanoparticles: Atomistic First-Principles Time-Dependent Density-Functional Theory Calculations. *Phys. Rev. B: Condens. Matter Mater. Phys.* **2015**, *91*, 115431.
(29) Rossi, T. P.; Zugarramurdi, A.; Puska, M. J.; Nieminen, R. M. Quantized Evolution of the Plasmonic Response in a Stretched Nanorod. *Phys. Rev. Lett.* **2015**, *115*, 236804.
(30) Marchesin, F.; Koval, P.; Barbry, M.; Aizpurua, J.; Sánchez-Portal, D. Plasmonic Response of Metallic Nanojunctions Driven by Single Atom Motion: Quantum Transport Revealed in Optics. *ACS Photonics* **2016**, *3*, 269.
(31) Donati, G.; Lingerfelt, D. B.; Aikens, C. M.; Li, X. Molecular Vibration Induced Plasmon Decay. *J. Phys. Chem. C* **2017**, *121*, 15368.
(32) Senanayake, R. D.; Lingerfelt, D. B.; Kuda-Singappulige, G. U.; Li, X.; Aikens, C. M. Real-Time TDDFT Investigation of Optical Absorption in Gold Nanowires. *J. Phys. Chem. C* **2019**, *123*, 14734.
(33) Ma, J.; Wang, Z.; Wang, L.-W. Interplay between Plasmon and Single-Particle Excitations in a Metal Nanocluster. *Nat. Commun.* **2015**, *6*, 10107.
(34) Douglas-Gallardo, O. A.; Berdakin, M.; Sánchez, C. G. Atomistic Insights into Chemical Interface Damping of Surface Plasmon Excitations in Silver Nanoclusters. *J. Phys. Chem. C* **2016**, *120*, 24389.
(35) Douglas-Gallardo, O. A.; Berdakin, M.; Frauenheim, T.; Sánchez, C. G. Plasmon-Induced Hot-Carrier Generation Differences in Gold and Silver Nanoclusters. *Nanoscale* **2019**, *11*, 8604.
(36) Hohenberg, P.; Kohn, W. Inhomogeneous Electron Gas. *Phys. Rev.* **1964**, *136*, B864.
(37) Kohn, W.; Sham, L. J. Self-Consistent Equations including Exchange and Correlation Effects. *Phys. Rev.* **1965**, *140*, A1133.
(38) Runge, E.; Gross, E. K. U. Density-Functional Theory for Time-Dependent Systems. *Phys. Rev. Lett.* **1984**, *52*, 997.
(39) Rossi, T. P.; Kuisma, M.; Puska, M. J.; Nieminen, R. M.; Erhart, P. Kohn–Sham Decomposition in Real-Time Time-Dependent Density-Functional Theory: An Efficient Tool for Analyzing Plasmonic Excitations. *J. Chem. Theory Comput.* **2017**, *13*, 4779.
(40) Gritsenko, O.; van Leeuwen, R.; van Lenthe, E.; Baerends, E. J. Self-Consistent Approximation to the Kohn-Sham Exchange Potential. *Phys. Rev. A: At., Mol., Opt. Phys.* **1995**, *51*, 1944.
(41) Kuisma, M.; Ojanen, J.; Enkovaara, J.; Rantala, T. Kohn-Sham Potential with Discontinuity for Band Gap Materials. *Phys. Rev. B: Condens. Matter Mater. Phys.* **2010**, *82*, 115106.
(42) Yan, J.; Jacobsen, K. W.; Thygesen, K. S. First-Principles Study of Surface Plasmons on Ag(111) and H/Ag(111). *Phys. Rev. B: Condens. Matter Mater. Phys.* **2011**, *84*, 235430.
(43) Yannouleas, C.; Broglia, R. Landau Damping and Wall Dissipation in Large Metal Clusters. *Ann. Phys.* **1992**, *217*, 105.
(44) Bernadotte, S.; Evers, F.; Jacob, C. R. Plasmons in Molecules. *J. Phys. Chem. C* **2013**, *117*, 1863.
(45) Yannouleas, C.; Broglia, R. A.; Brack, M.; Bortignon, P. F. Fragmentation of the Photoabsorption Strength in Neutral and Charged Metal Microclusters. *Phys. Rev. Lett.* **1989**, *63*, 255.
(46) Yannouleas, C.; Broglia, R. A. Collective and Single-Particle Aspects in the Optical Response of Metal Microclusters. *Phys. Rev. A: At., Mol., Opt. Phys.* **1991**, *44*, 5793.
(47) You, X.; Ramakrishna, S.; Seideman, T. Origin of Plasmon Lineshape and Enhanced Hot Electron Generation in Metal Nanoparticles. *J. Phys. Chem. Lett.* **2018**, *9*, 141.
(48) Zhang, R.; Bursi, L.; Cox, J. D.; Cui, Y.; Krauter, C. M.; Alabastri, A.; Manjavacas, A.; Calzolari, A.; Corni, S.; Molinari, E.; Carter, E. A.; García de Abajo, F. J.; Zhang, H.; Nordlander, P. How to Identify Plasmons from the Optical Response of Nanostructures. *ACS Nano* **2017**, *11*, 7321.
(49) Hartland, G. V.; Besteiro, L. V.; Johns, P.; Govorov, A. O. What's So Hot about Electrons in Metal Nanoparticles? *ACS Energy Lett.* **2017**, *2*, 1641.
(50) Aizpurua, J.; Baletto, F.; Baumberg, J.; Christopher, P.; Nijs, B. d.; Deshpande, P.; Diaz Fernandez, Y.; Fabris, L.; Freakley, S.; Gawinkowski, S.; Govorov, A.; Halas, N.; Hernandez, R.; Jankiewicz, B.; Khurgin, J.; Kuisma, M.; Kumar, P. V.; Lischner, J.; Liu, J.; Marini, A.; et al. Theory of Hot Electrons: General Discussion. *Faraday Discuss.* **2019**, *214*, 245.
(51) Khurgin, J. B. Fundamental Limits of Hot Carrier Injection from Metal in Nanoplasmonics. *Nanophotonics* **2020**, *9*, 453.
(52) Brown, A. M.; Sundararaman, R.; Narang, P.; Goddard, W. A.; Atwater, H. A. Nonradiative Plasmon Decay and Hot Carrier Dynamics: Effects of Phonons, Surfaces, and Geometry. *ACS Nano* **2016**, *10*, 957.
(53) Narang, P.; Sundararaman, R.; Atwater, H. A. Plasmonic Hot Carrier Dynamics in Solid-State and Chemical Systems for Energy Conversion. *Nanophotonics* **2016**, *5*, 96.
(54) Christopher, P.; Moskovits, M. Hot Charge Carrier Transmission from Plasmonic Nanostructures. *Annu. Rev. Phys. Chem.* **2017**, *68*, 379.
(55) Wu, K.; Chen, J.; McBride, J. R.; Lian, T. Efficient Hot-Electron Transfer by a Plasmon-Induced Interfacial Charge-Transfer Transition. *Science* **2015**, *349*, 632.
(56) Kale, M. J.; Christopher, P. Plasmons at the Interface. *Science* **2015**, *349*, 587.
(57) Boerigter, C.; Campana, R.; Morabito, M.; Linic, S. Evidence and Implications of Direct Charge Excitation as the Dominant Mechanism in Plasmon-Mediated Photocatalysis. *Nat. Commun.* **2016**, *7*, 10545.
(58) Boerigter, C.; Aslam, U.; Linic, S. Mechanism of Charge Transfer from Plasmonic Nanostructures to Chemically Attached Materials. *ACS Nano* **2016**, *10*, 6108.
(59) Tan, S.; Argondizzo, A.; Ren, J.; Liu, L.; Zhao, J.; Petek, H. Plasmonic Coupling at a Metal/Semiconductor Interface. *Nat. Photonics* **2017**, *11*, 806.
(60) Tan, S.; Dai, Y.; Zhang, S.; Liu, L.; Zhao, J.; Petek, H. Coherent Electron Transfer at the Ag/Graphite Heterojunction Interface. *Phys. Rev. Lett.* **2018**, *120*, 126801.
(61) Li, Y.; DiStefano, J. G.; Murthy, A. A.; Cain, J. D.; Hanson, E. D.; Li, Q.; Castro, F. C.; Chen, X.; Dravid, V. P. Superior Plasmonic Photodetectors Based on Au@MoS_2 Core-Shell Heterostructures. *ACS Nano* **2017**, *11*, 10321.
(62) Foerster, B.; Joplin, A.; Kaefer, K.; Celiksoy, S.; Link, S.; Sönnichsen, C. Chemical Interface Damping Depends on Electrons Reaching the Surface. *ACS Nano* **2017**, *11*, 2886.
(63) Ratchford, D. C.; Dunkelberger, A. D.; Vurgaftman, I.; Owrutsky, J. C.; Pehrsson, P. E. Quantification of Efficient Plasmonic Hot-Electron Injection in Gold Nanoparticle-TiO_2 Films. *Nano Lett.* **2017**, *17*, 6047.
(64) Tan, S.; Liu, L.; Dai, Y.; Ren, J.; Zhao, J.; Petek, H. Ultrafast Plasmon-Enhanced Hot Electron Generation at Ag Nanocluster/Graphite Heterojunctions. *J. Am. Chem. Soc.* **2017**, *139*, 6160.
(65) Brown, A. M.; Sundararaman, R.; Narang, P.; Schwartzberg, A. M.; Goddard, W. A.; Atwater, H. A. Experimental and *Ab Initio* Ultrafast Carrier Dynamics in Plasmonic Nanoparticles. *Phys. Rev. Lett.* **2017**, *118*, No. 087401.
(66) Besteiro, L. V.; Kong, X.-T.; Wang, Z.; Hartland, G.; Govorov, A. O. Understanding Hot-Electron Generation and Plasmon Relaxation in

https://dx.doi.org/10.1021/acsnano.0c03004
ACS Nano 2020, 14, 9963–9971

Metal Nanocrystals: Quantum and Classical Mechanisms. *ACS Photonics* **2017**, *4*, 2759.
(67) Kumar, P. V.; Rossi, T. P.; Kuisma, M.; Erhart, P.; Norris, D. J. Direct Hot-Carrier Transfer in Plasmonic Catalysis. *Faraday Discuss.* **2019**, *214*, 189.
(68) Kumar, P. V.; Rossi, T. P.; Marti-Dafcik, D.; Reichmuth, D.; Kuisma, M.; Erhart, P.; Puska, M. J.; Norris, D. J. Plasmon-Induced Direct Hot-Carrier Transfer at Metal-Acceptor Interfaces. *ACS Nano* **2019**, *13*, 3188.
(69) Ma, J.; Gao, S. Plasmon-Induced Electron−Hole Separation at the Ag/TiO_2(110) Interface. *ACS Nano* **2019**, *13*, 13658.
(70) Enkovaara, J.; Rostgaard, C.; Mortensen, J. J.; Chen, J.; Dulak, M.; Ferrighi, L.; Gavnholt, J.; Glinsvad, C.; Haikola, V.; Hansen, H. A.; Kristoffersen, H. H.; Kuisma, M.; Larsen, A. H.; Lehtovaara, L.; Ljungberg, M.; Lopez-Acevedo, O.; Moses, P. G.; Ojanen, J.; Olsen, T.; Petzold, V.; et al. Electronic Structure Calculations with GPAW: A Real-Space Implementation of the Projector Augmented-Wave Method. *J. Phys.: Condens. Matter* **2010**, *22*, 253202.
(71) Larsen, A. H.; Vanin, M.; Mortensen, J. J.; Thygesen, K. S.; Jacobsen, K. W. Localized Atomic Basis Set in the Projector Augmented Wave Method. *Phys. Rev. B: Condens. Matter Mater. Phys.* **2009**, *80*, 195112.
(72) Blöchl, P. E. Projector Augmented-Wave Method. *Phys. Rev. B: Condens. Matter Mater. Phys.* **1994**, *50*, 17953.
(73) Rossi, T. P.; Lehtola, S.; Sakko, A.; Puska, M. J.; Nieminen, R. M. Nanoplasmonics Simulations at the Basis Set Limit through Completeness-Optimized, Local Numerical Basis Sets. *J. Chem. Phys.* **2015**, *142*, No. 094114.
(74) Yabana, K.; Bertsch, G. F. Time-Dependent Local-Density Approximation in Real Time. *Phys. Rev. B: Condens. Matter Mater. Phys.* **1996**, *54*, 4484.
(75) Larsen, A.; Mortensen, J.; Blomqvist, J.; Castelli, I.; Christensen, R.; Dulak, M.; Friis, J.; Groves, M.; Hammer, B.; Hargus, C.; Hermes, E.; Jennings, P.; Jensen, P.; Kermode, J.; Kitchin, J.; Kolsbjerg, E.; Kubal, J.; Kaasbjerg, K.; Lysgaard, S.; Maronsson, J.; et al. The Atomic Simulation Environment − A Python Library for Working with Atoms. *J. Phys.: Condens. Matter* **2017**, *29*, 273002.
(76) Perdew, J. P.; Burke, K.; Ernzerhof, M. Generalized Gradient Approximation Made Simple. *Phys. Rev. Lett.* **1996**, *77*, 3865.
(77) Casida, M. E. Time-Dependent Density Functional Response Theory for Molecules. In *Recent Advances in Density Functional Methods, Part I*; Chong, D. P., Ed.; World Scientific: Singapore, 1995; p 155.
(78) Mortensen, J. J.; Hansen, L. B.; Jacobsen, K. W. Real-Space Grid Implementation of the Projector Augmented Wave Method. *Phys. Rev. B: Condens. Matter Mater. Phys.* **2005**, *71*, No. 035109.
(79) van der Walt, S.; Colbert, S. C.; Varoquaux, G. The NumPy Array: A Structure for Efficient Numerical Computation. *Comput. Sci. Eng.* **2011**, *13*, 22.
(80) Hunter, J. D. Matplotlib: A 2D Graphics Environment. *Comput. Sci. Eng.* **2007**, *9*, 90.
(81) Humphrey, W.; Dalke, A.; Schulten, K. VMD − Visual Molecular Dynamics. *J. Mol. Graphics* **1996**, *14*, 33.
(82) Stone, J. An Efficient Library for Parallel Ray Tracing and Animation. M.Sc. Thesis, University of Missouri-Rolla, 1998.

https://dx.doi.org/10.1021/acsnano.0c03004
ACS Nano 2020, 14, 9963−9971

Supporting Information

Hot-Carrier Generation in Plasmonic Nanoparticles: The Importance of Atomic Structure

Tuomas P. Rossi,† Paul Erhart,† and Mikael Kuisma‡

† *Department of Physics, Chalmers University of Technology, SE-412 96 Gothenburg, Sweden*
‡ *Department of Chemistry, Nanoscience Center, University of Jyväskylä, FI-40014 Jyväskylä, Finland*

Contents

Supplementary Figures

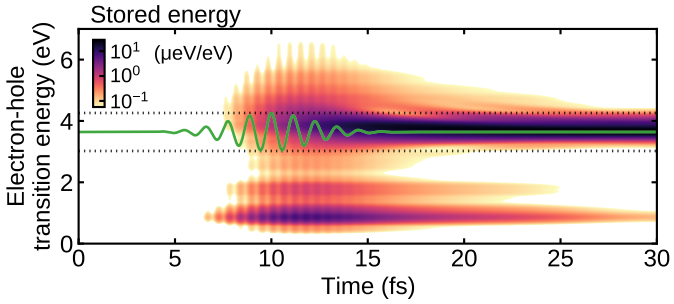

Supplementary Figure S1: Distribution of the stored energy over electron-hole transition energies in Ag_{561}. Distribution of the stored energy $E_{ia}(t)$ (Supplementary Note S1) over electron-hole transition energies ω_{ia}, *i.e.*, $E(\omega, t) = \sum_{ia} E_{ia}(t)\delta(\omega - \omega_{ia})$ with a Gaussian smoothing over ω is shown. The color scale is logarithmic. The pulse is overlaid at its frequency ω_0 and the pulse width $\sigma = \sqrt{2}/\tau_0$ is indicated as dotted lines at $\omega_0 \pm 2\sigma$. The contribution from resonant transitions in Fig. 1e in the main text comprises of transitions with energy ω_{ia} between $\omega_0 \pm 2\sigma$, and that from the non-resonant transitions comprises of the plasmonic low-energy transitions ($\omega_{ia} < \omega_0 - 2\sigma$) and the screening high-energy transitions ($\omega_{ia} > \omega_0 + 2\sigma$).

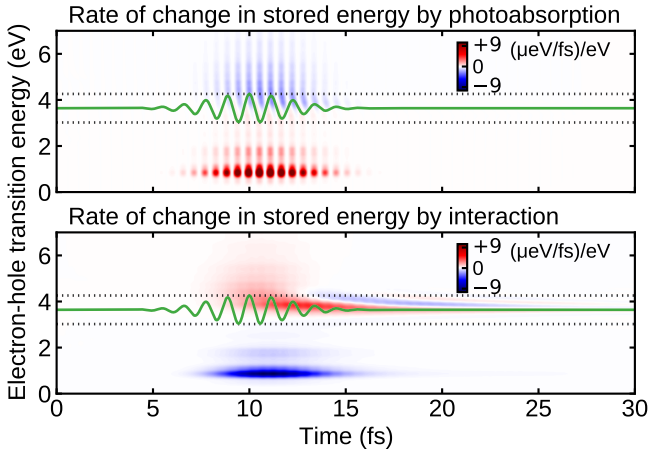

Supplementary Figure S2: Rate of change in energy stored in Ag_{561}. Distributions of the rate of change $\dot{E}_{ia}(t)$ over electron-hole transition energies ω_{ia} divided into photoabsorption and interaction components (Supplementary Note S3). The plasmonic low-energy transitions absorb the energy from the resonant pulse (upper panel) and the energy is subsequently redistributed to higher-energy screening transitions and resonant hot-carrier transitions (lower panel). The screening transitions return their energy back to the field weakening the photoabsorption by plasmon (upper panel), and after the plasmon has dephased, the absorbed energy remains in hot-carrier transitions.

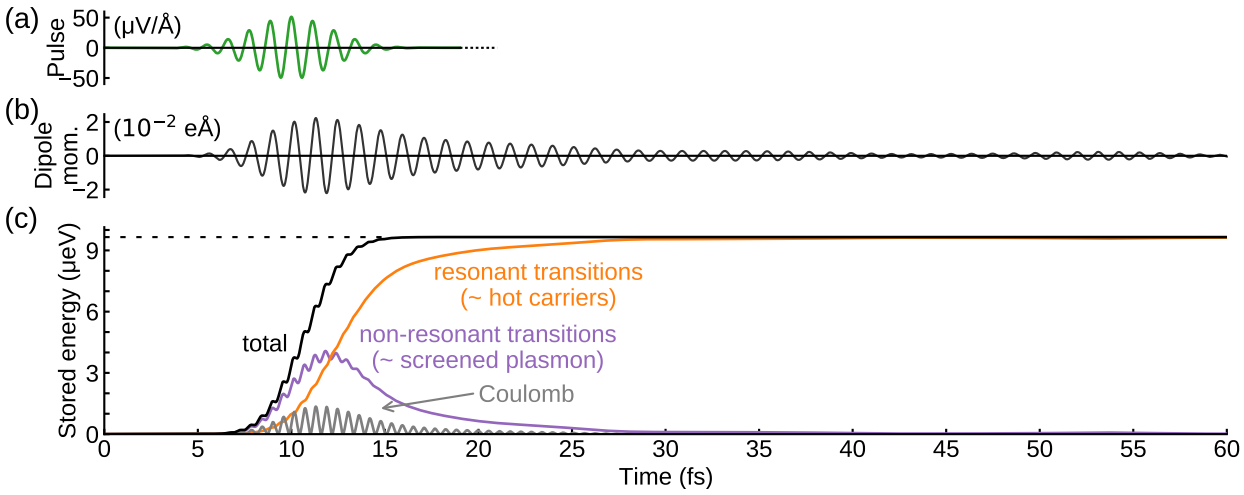

Supplementary Figure S3: Real-time dynamics in Ag_{561} up to 60 fs. (a) Electric field pulse impacting the nanoparticle. (b) Time-dependent dipole moment response of the nanoparticle. (c) Time evolution of the energy stored in the excited electronic system divided into non-resonant and resonant contributions as in Fig. 1 in the main text. The plasmon has dephased at 30 fs and only a minor recurrence of the plasmon is visible at around 55 fs.

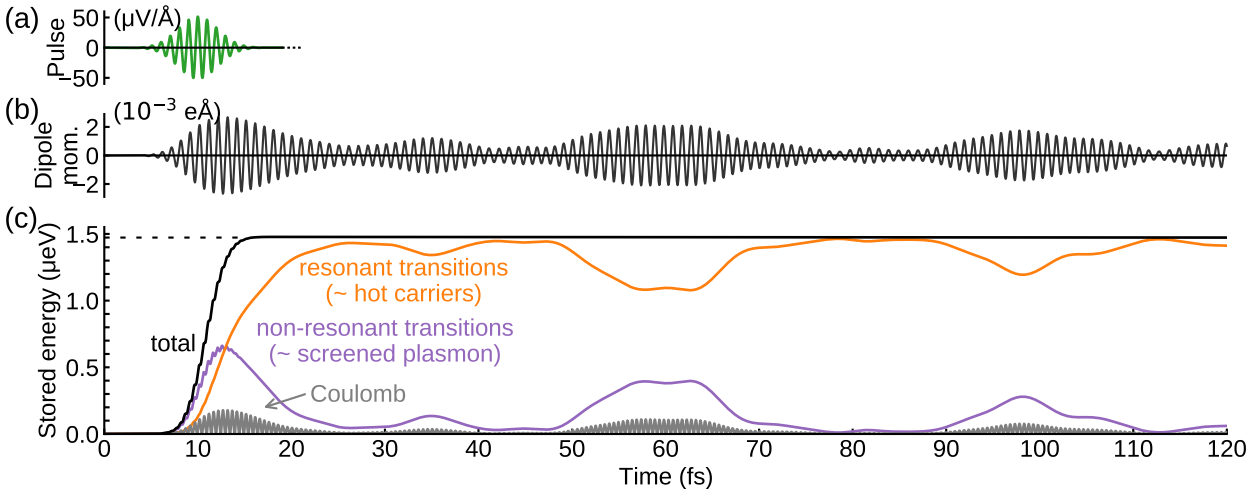

Supplementary Figure S4: Real-time dynamics in Ag_{55} up to 120 fs. (a) Electric field pulse impacting the nanoparticle. (c) Time-dependent dipole moment response of the nanoparticle. (e) Time evolution of the energy stored in the excited electronic system divided into non-resonant and resonant contributions analogously to Fig. 1 in the main text. The response of Ag_{55} consists of a few separate resonances instead of a single broad one, which appears in the time-domain as Rabi oscillations and recurrence of the plasmon. At long time scales, the dynamics is expected to be affected by electron–electron interaction and other scattering processes that lead to excitation decay but are not included in the present description.

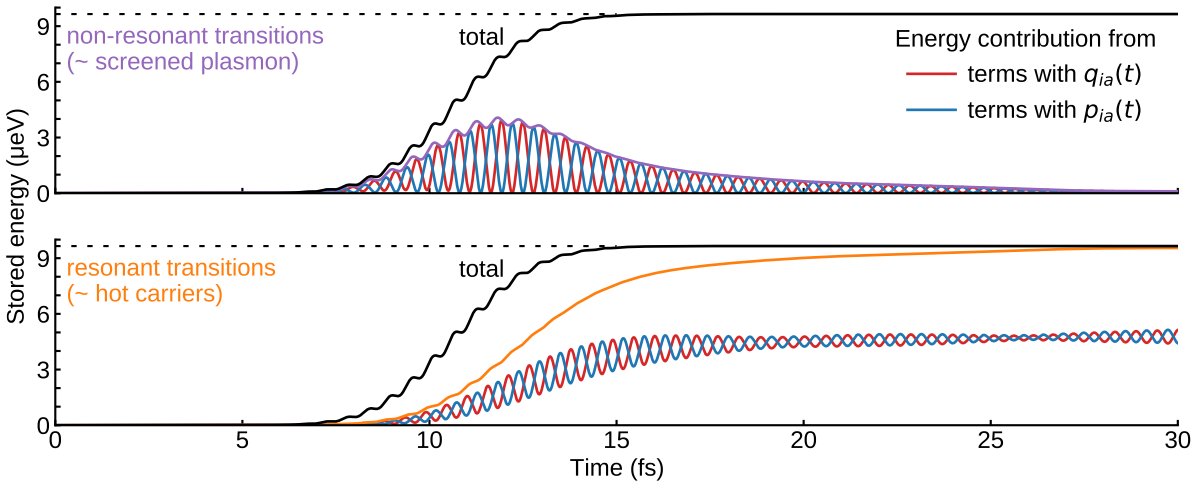

Supplementary Figure S5: Energy contributions from real and imaginary parts of density matrix. The energy stored in non-resonant and resonant transitions (Fig. 1 in main text) is further decomposed to contributions from the real and imaginary parts of density matrix, *i.e.*, from $q_{ia}(t)$ and $p_{ia}(t)$ defined in Eq. (33), respectively. Specifically, terms with $q_{ia}(t)$ are $\frac{1}{2}\omega_{ia}q_{ia}^2(t) + \frac{1}{2}q_{ia}(t)\sum_{jb}K_{ia,jb}q_{jb}(t)$ and terms with $p_{ia}(t)$ are $\frac{1}{2}\omega_{ia}p_{ia}^2(t)$, summing up to the energy $E_{ia}(t)$ in Eq. (35). The upper panel illustrates that plasmon can be thought as a classical harmonic oscillator with energy oscillating between density (q_{ia} or "position coordinate") and current (p_{ia} or "momentum coordinate").

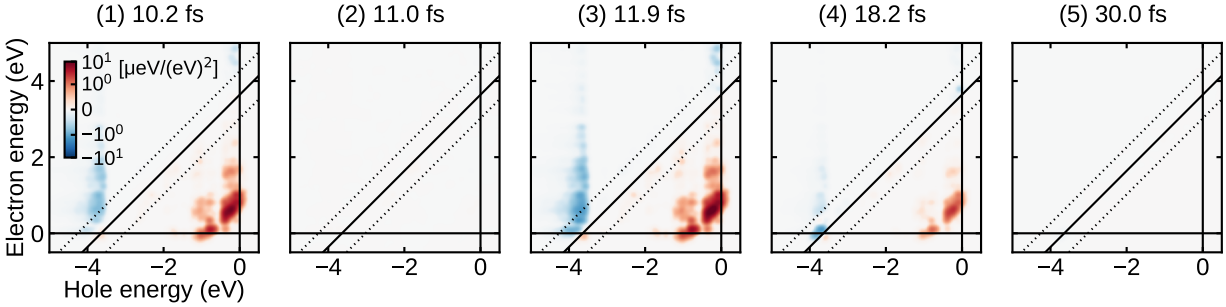

Supplementary Figure S6: Electron-hole transition contributions to Coulomb energy. The contributions are visualized as TCM on a logarithmic color scale similarly to the total energy in Fig. 2 in the main text. Note that while the screening high-energy transitions have negative contribution to the Coulomb energy, the total energy contribution from every electron-hole transition is positive as depicted in Fig. 2 in the main text. See Eq. (35) and discussion therein for the energy terms.

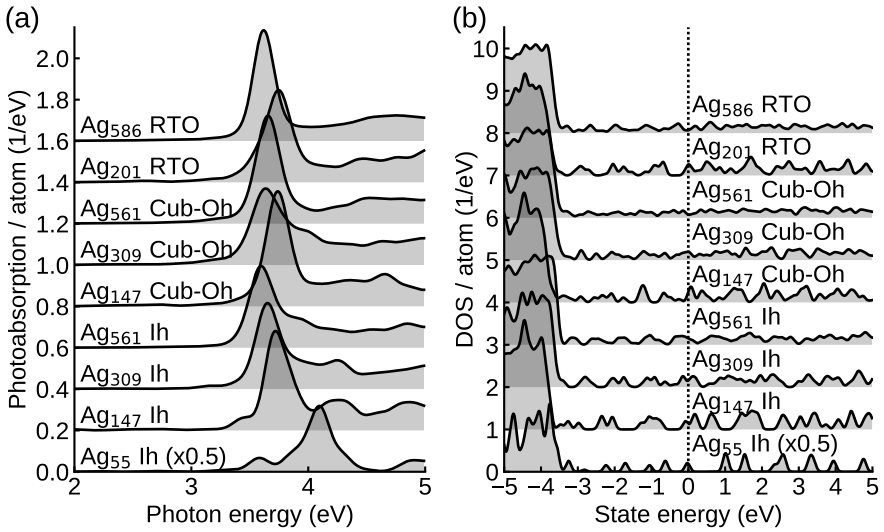

Supplementary Figure S7: Photoabsorption spectra and densities of states of silver nanoparticles. (a) Photoabsorption spectra and (b) densities of states (DOS) of silver nanoparticles of icosahedral (Ih), cuboctahedral (Cub-Oh), and regularly truncated octahedral (RTO) shapes. The Fermi level is at 0 eV in panel b. The data for Ag_{55} has been multiplied by 0.5. For each shape, the plasmon resonance show a redshift with increasing particle size, following the shift in the d-band onset with respect to the Fermi level apart from the small Ag_{55}. Ag_{309} Cub-Oh is an exception with broader and more redshifted plasmon peak than expected based on Ag_{147} and Ag_{561}, with a corresponding difference seen in the d-band onset.

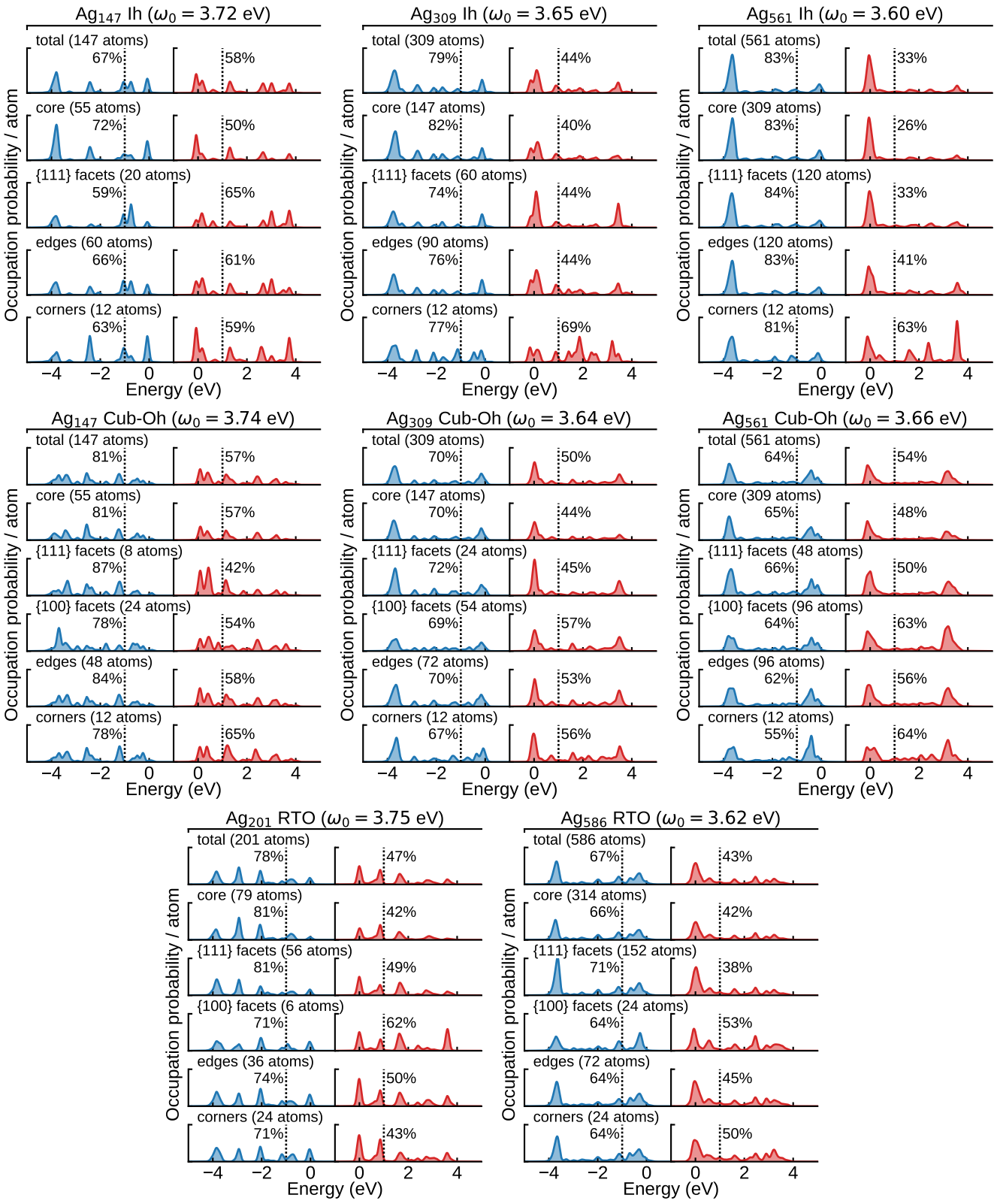

Supplementary Figure S8: Hot-carrier distributions in silver nanoparticles. Occupation probabilities of hole and electron states after plasmon decay in silver nanoparticles of icosahedral (Ih), cuboctahedral (Cub-Oh), and regularly truncated octahedral (RTO) shapes. Occupation probabilities at different atomic sites (core, facets, edges, and corners) are also shown. The distributions are per atom (the number of atoms in each set is indicated in parenthesis). The percentages adjacent to the −1 eV and 1 eV dotted lines indicate the amount of holes and electrons with energy < -1 eV and > 1 eV, respectively, in comparison to the total amount in each set. Scale is the same in each plot.

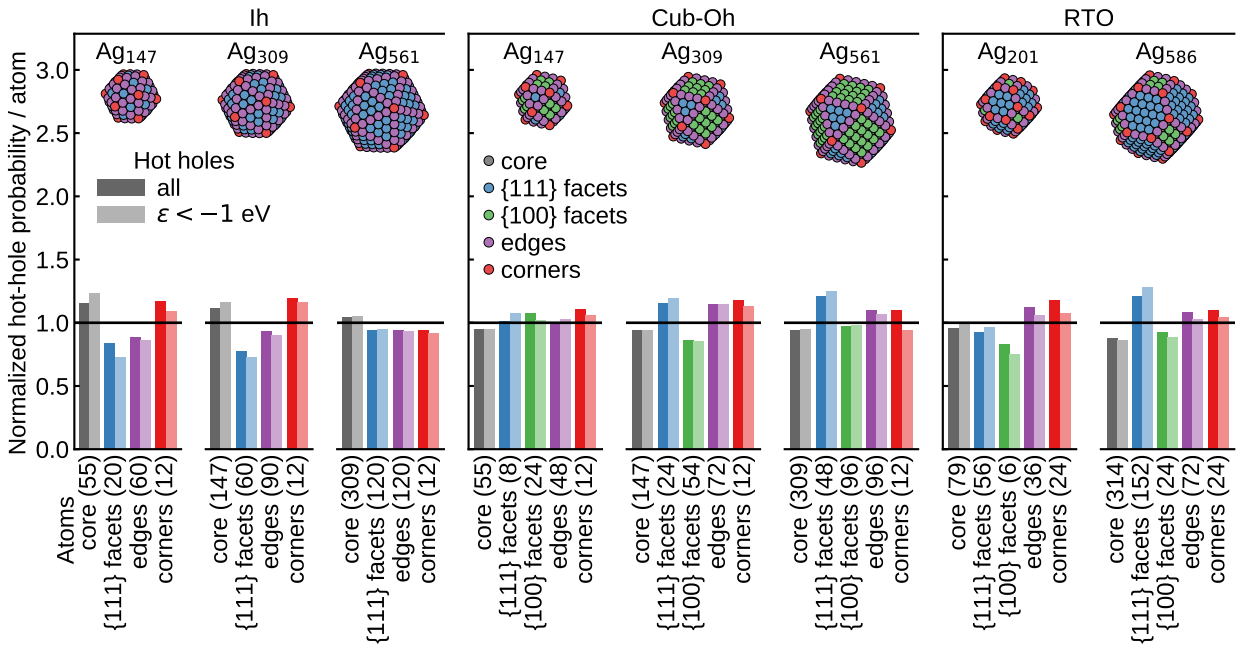

Supplementary Figure S9: Atomic-scale distributions of hot holes in silver nanoparticles. Spatial distribution of hot holes generated on different atomic sites in selected nanoparticles. Most distributions show relatively small variations from spatially uniform distribution and no surface or core site appear to be systematically favored. The distribution of hotter holes (energy $\epsilon < -1$ eV) is similar to that of all generated holes due to the d electron states dominating the hot-hole distribution (Supplementary Fig. S8).

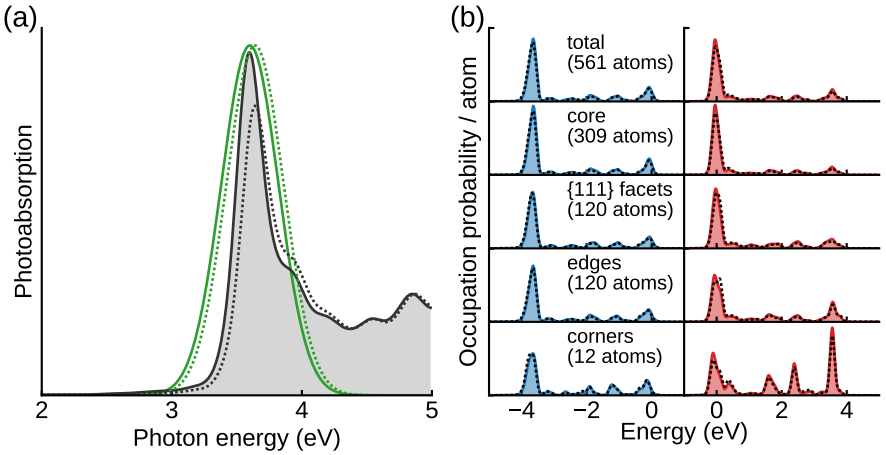

Supplementary Figure S10: Effect of the dynamic response kernel on the results. (a) Photoabsorption spectra of Ag_{561} calculated with the adiabatic GLLB-sc exchange-correlation (XC) potential (solid shaded black line) and random-phase approximation (RPA) (dotted black line). The pulse is tuned to the plasmon resonance (3.60 eV for the adiabatic GLLB-sc and 3.64 eV for RPA; solid and dashed green lines, respectively). (b) Hot-carrier distributions in Ag_{561} calculated with the adiabatic GLLB-sc (solid shaded lines) and RPA (dotted lines). The ground state is calculated with GLLB-sc XC potential in all the cases. The differences in the results obtained with different dynamic response kernels are minor.

Supplementary Notes

Supplementary Note S1: Perturbation expansions of time-dependent quantities.

Wave function. The expansion of the time-dependent wave function up to second order in perturbation is (notation: $|i(t)\rangle = \psi_i(t)$ and $|i\rangle = \psi_i^{(0)}$)

$$|i(t)\rangle = e^{-i\epsilon_i t}\,|i\rangle + \sum_j e^{-i\epsilon_j t} C_{ji}^{(1)}(t)\,|j\rangle + \sum_j e^{-i\epsilon_j t} C_{ji}^{(2)}(t)\,|j\rangle\,, \tag{1}$$

which gives the projection $\langle k|i(t)\rangle = e^{-i\epsilon_k t}\left(\delta_{ik} + C_{ki}^{(1)}(t) + C_{ki}^{(2)}(t)\right)$. Consider the norm up to second order

$$\langle j(t)|i(t)\rangle = \sum_k \langle j(t)|k\rangle\,\langle k|i(t)\rangle = \delta_{ji} + \underbrace{C_{ji}^{(1)}(t) + C_{ij}^{(1)*}(t)}_{=0} + \underbrace{C_{ji}^{(2)}(t) + C_{ij}^{(2)*}(t) + \sum_k C_{kj}^{(1)*}(t) C_{ki}^{(1)}(t)}_{=0}, \tag{2}$$

where the denoted first and second order terms are required to vanish in order to have unitary evolution, *i.e.*, $\langle j(t)|i(t)\rangle = \delta_{ji}$.

Density matrix. The expansion of the time-dependent Kohn–Sham density matrix is

$$\rho_{mn}(t) = \sum_i \langle n|i(t)\rangle\, f_i\, \langle i(t)|m\rangle \tag{3}$$

$$= f_n\delta_{nm} + e^{-i(\epsilon_n-\epsilon_m)t}\left[\left(f_n C_{mn}^{(1)*}(t) + f_m C_{nm}^{(1)}(t)\right) + \left(f_n C_{mn}^{(2)*}(t) + f_m C_{nm}^{(2)}(t) + \sum_i f_i C_{ni}^{(1)}(t) C_{mi}^{(1)*}(t)\right)\right] \tag{4}$$

By invoking the conditions from unitary evolution from Eq. (2), the first-order contribution simplifies to

$$\rho_{mn}^{(1)}(t) = e^{-i(\epsilon_n-\epsilon_m)t}(f_m - f_n) C_{nm}^{(1)}(t). \tag{5}$$

Note that in the first order the electron-electron and hole-hole parts of the density matrix are zero: $\rho_{mn}^{(1)}(t) = 0$ for $f_m = f_n$, including the diagonal $\rho_{nn}^{(1)}(t) = 0$.

The leading second-order term of the electron-electron and hole-hole parts is obtained by setting $f_m = f_n$ and using Eqs. (2) and (5) as

$$\rho_{mn}^{(2)}(t) = e^{-i(\epsilon_n-\epsilon_m)t}\left[f_n\left(C_{mn}^{(2)*}(t) + C_{nm}^{(2)}(t)\right) + \sum_i f_i C_{ni}^{(1)}(t) C_{mi}^{(1)*}(t)\right] \tag{6}$$

$$= \sum_i e^{-i(\epsilon_n-\epsilon_m)t}(f_i - f_n) C_{mi}^{(1)*}(t) C_{ni}^{(1)}(t) \tag{7}$$

$$= \sum_i^{f_i\neq f_n} \frac{1}{f_i - f_n}\rho_{in}^{(1)}(t)\rho_{im}^{(1)*}(t) \tag{8}$$

$$= \sum_i^{f_i>f_n} \frac{\rho_{in}^{(1)}(t)}{\sqrt{f_i - f_n}}\frac{\rho_{im}^{(1)*}(t)}{\sqrt{f_i - f_m}} - \sum_i^{f_i<f_n} \frac{\rho_{in}^{(1)}(t)}{\sqrt{f_n - f_i}}\frac{\rho_{im}^{(1)*}(t)}{\sqrt{f_m - f_i}}, \tag{9}$$

the first and second terms of which constitute the electron-electron and hole-hole parts of the density matrix. In particular, the diagonal can be simplified by noting that $|\rho_{in}^{(1)}(t)|^2 = |\rho_{ni}^{(1)}(t)|^2$ to

$$\rho_{nn}^{(2)}(t) = \sum_i^{f_i>f_n}\left|\frac{\rho_{in}^{(1)}(t)}{\sqrt{f_i - f_n}}\right|^2 - \sum_i^{f_i<f_n}\left|\frac{\rho_{ni}^{(1)}(t)}{\sqrt{f_n - f_i}}\right|^2. \tag{10}$$

By defining transition probability

$$P_{ia}(t) = \left|\frac{\delta\rho_{ia}(t)}{\sqrt{f_i - f_a}}\right|^2, \tag{11}$$

Eq. (10) reads

$$\rho^{(2)}_{nn}(t) = \sum_{i}^{f_i>f_n} P_{in}(t) - \sum_{a}^{f_n>f_a} P_{na}(t) = P^{\mathrm{e}}_n(t) - P^{\mathrm{h}}_n(t), \tag{12}$$

where $P^{\mathrm{e}}_n(t)$ and $P^{\mathrm{h}}_n(t)$ corresponds to induced occupations of electrons and holes on state n, respectively.

Energy. In the Kohn–Sham density-functional theory, the total energy is composed of kinetic, Hartree, and XC contributions, and of the external potential energy (including the potential created by nuclei v^{ext} and first-order light pulse v^{pulse}),

$$E_{\mathrm{tot}}(t) = T(t) + E_{\mathrm{H}}(t) + E_{\mathrm{xc}}(t) + E_{\mathrm{ext}}(t), \tag{13}$$

respectively. In the basis of KS states, these energy terms are (assuming adiabatic XC kernel)

$$T(t) = \sum_n f_n \int \mathrm{d}\boldsymbol{r} \psi^*_n(\boldsymbol{r},t) \left(-\frac{1}{2}\nabla^2\right) \psi_n(\boldsymbol{r},t) \tag{14}$$

$$= \sum_{ij} \rho_{ij}(t) t_{ij}, \tag{15}$$

$$E_{\mathrm{H}}(t) = \frac{1}{2} \int \mathrm{d}\boldsymbol{r} \int \mathrm{d}\boldsymbol{r}' n(\boldsymbol{r},t) \frac{1}{|\boldsymbol{r}-\boldsymbol{r}'|} n(\boldsymbol{r}',t) \tag{16}$$

$$= \frac{1}{2} \sum_{ij,kl} \rho_{ij}(t) K^{\mathrm{H}}_{ij,kl} \rho_{kl}(t), \tag{17}$$

$$E_{\mathrm{xc}}(t) = E^{(0)}_{\mathrm{xc}} + \int \mathrm{d}\boldsymbol{r} v_{\mathrm{xc}}(\boldsymbol{r}) \delta n(\boldsymbol{r},t) + \frac{1}{2} \int \mathrm{d}\boldsymbol{r} \int \mathrm{d}\boldsymbol{r}' \delta n(\boldsymbol{r},t) K^{\mathrm{xc}}(\boldsymbol{r},\boldsymbol{r}') \delta n(\boldsymbol{r}',t) + \dots \tag{18}$$

$$= E^{(0)}_{\mathrm{xc}} + \sum_{ij} \delta\rho_{ij}(t) v^{\mathrm{xc}}_{ij} + \frac{1}{2} \sum_{kl} \delta\rho_{ij}(t) K^{\mathrm{xc}}_{ij,kl} \delta\rho_{kl}(t) + \dots, \tag{19}$$

and

$$E_{\mathrm{ext}}(t) = \int \mathrm{d}\boldsymbol{r} n(\boldsymbol{r},t) \left[v^{\mathrm{ext}}(\boldsymbol{r}) + v^{\mathrm{pulse}}(\boldsymbol{r},t)\right] \tag{20}$$

$$= \sum_{ij} \rho_{ij}(t) \left[v^{\mathrm{ext}}_{ij} + v^{\mathrm{pulse}}_{ij}(t)\right], \tag{21}$$

where $\rho_{ij}(t) = \rho^{(0)}_{ij} + \rho^{(1)}_{ij}(t) + \rho^{(2)}_{ij}(t) + \dots$ and $\delta\rho_{ij}(t) = \rho_{ij}(t) - \rho^{(0)}_{ij}$. The perturbation expansions of the energy contributions are

$$T(t) = T^{(0)} + \sum_{ij} \rho^{(1)}_{ij}(t) t_{ij} + \sum_{ij} \rho^{(2)}_{ij}(t) t_{ij} \tag{22}$$

$$E_{\mathrm{H}}(t) = E^{(0)}_{\mathrm{H}} + \sum_{ij,kl} \rho^{(1)}_{ij}(t) K^{\mathrm{H}}_{ij,kl} \rho^{(0)}_{kl} + \sum_{ij,kl} \rho^{(2)}_{ij}(t) K^{\mathrm{H}}_{ij,kl} \rho^{(0)}_{kl} + \frac{1}{2} \sum_{ij,kl} \rho^{(1)}_{ij}(t) K^{\mathrm{H}}_{ij,kl} \rho^{(1)}_{kl}(t) \tag{23}$$

$$E_{\mathrm{xc}}(t) = E^{(0)}_{\mathrm{xc}} + \sum_{ij} \rho^{(1)}_{ij}(t) v^{\mathrm{xc}}_{ij} + \sum_{ij} \rho^{(2)}_{ij}(t) v^{\mathrm{xc}}_{ij} + \frac{1}{2} \sum_{ij,kl} \rho^{(1)}_{ij}(t) K^{\mathrm{xc}}_{ij,kl} \rho^{(1)}_{kl}(t) \tag{24}$$

$$E_{\mathrm{ext}}(t) = V^{(0)}_{\mathrm{ext}} + \sum_{ij} \rho^{(1)}_{ij}(t) v^{\mathrm{ext}}_{ij} + \rho^{(0)}_{ij} v^{\mathrm{pulse}}_{ij}(t) + \sum_{ij} \rho^{(2)}_{ij}(t) v^{\mathrm{ext}}_{ij} + \rho^{(1)}_{ij}(t) v^{\mathrm{pulse}}_{ij}(t) \tag{25}$$

(note that here the summations over ij and kl run over all indices, including both the electron-hole and hole-electron spaces and the diagonal).

The first order gives

$$E^{(1)}_{\mathrm{tot}}(t) = \sum_{ij} \rho^{(1)}_{ij}(t) \left[t_{ij} + \sum_{kl} K^{\mathrm{H}}_{ij,kl} \rho^{(0)}_{kl} + v^{\mathrm{xc}}_{ij} + v^{\mathrm{ext}}_{ij}\right] + \rho^{(0)}_{ij} v^{\mathrm{pulse}}_{ij}(t) = \underbrace{\sum_{ij} \rho^{(1)}_{ij}(t) H^{(0)}_{ij}}_{=0} - \mu^{(0)} \mathcal{E}(t), \tag{26}$$

where the first term vanishes as the ground-state Hamiltonian $H^{(0)}_{ij} = \epsilon_i \delta_{ij}$ and $\rho^{(1)}_{ii}(t) = 0$.

The second order gives

$$E^{(2)}_{\rm tot}(t) = \sum_{ij} \rho^{(2)}_{ij}(t) \left[t_{ij} + \sum_{kl} K^{\rm H}_{ij,kl} \rho^{(0)}_{kl} + v^{\rm xc}_{ij} + v^{\rm ext}_{ij} \right] + \frac{1}{2} \sum_{ij,kl} \rho^{(1)}_{ij}(t) \left(K^{\rm H}_{ij,kl} + K^{\rm xc}_{ij,kl} \right) \rho^{(1)}_{kl}(t) + \sum_{ij} \rho^{(1)}_{ij}(t) v^{\rm pulse}_{ij}(t) \quad (27)$$

$$= \sum_{i} \rho^{(2)}_{ii}(t) \epsilon_i + \frac{1}{2} \sum_{ij,kl} \rho^{(1)}_{ij}(t) K^{\rm Hxc}_{ij,kl} \rho^{(1)}_{kl}(t) - \mu^{(1)}(t) \mathcal{E}(t). \quad (28)$$

By using Eq. (12) and assuming real-valued ground-state KS wave functions and frequency-independent XC kernel, simplifying the Hartree-XC term, [1] Eq. (28) can be written as a sum over electron-hole space only

$$E^{(2)}_{\rm tot}(t) = \underbrace{\sum_{ia}^{f_i > f_a} \left[\omega_{ia} P_{ia}(t) + \underbrace{\frac{1}{2} \cdot 2\Re \rho^{(1)}_{ia}(t) \sum_{jb}^{f_j > f_b} K^{\rm Hxc}_{ia,jb} 2\Re \rho^{(1)}_{jb}(t)}_{=E^{\rm C}_{ia}(t)} \right]}_{=E_{ia}(t)} - \mu^{(1)}(t) \mathcal{E}(t), \quad (29)$$

where the Hartree-XC term is used to estimate the Coulomb energy $E^{\rm C}_{ia}(t)$. In RPA, the XC is neglected and $K^{\rm Hxc}$ is replaced by the Hartree kernel $K^{\rm H}(\boldsymbol{r}, \boldsymbol{r}') = |\boldsymbol{r} - \boldsymbol{r}'|^{-1}$.

By collecting all the terms, the energy up to the second order is

$$E_{\rm tot}(t) = E^{(0)}_{\rm tot} + \sum_{ia}^{f_i > f_a} E_{ia}(t) - \underbrace{\left[\mu^{(0)} + \mu^{(1)}(t) \right] \mathcal{E}(t)}_{=\mu(t)\mathcal{E}(t) = -E_{\rm pulse}(t)}. \quad (30)$$

Supplementary Note S2: Energy in terms of real and imaginary parts of density matrix.

The real and imaginary parts of the time-dependent density matrix have a well-defined connection [Eq. (4.25) of Ref. 1]. By assuming real-valued ground-state wave functions and a frequency-independent XC kernel, the connection can be expressed in electron-hole space in the time domain as

$$\begin{cases} \Re \delta \dot{\rho}_{ia}(t) = -\omega_{ia} \Im \delta \rho_{ia}(t) \\ \Im \delta \dot{\rho}_{ia}(t) = \omega_{ia} \Re \delta \rho_{ia}(t) + (f_i - f_a) \sum_{jb}^{f_j > f_b} K^{\rm Hxc}_{ia,jb} 2\Re \delta \rho_{jb}(t) + (f_i - f_a) v^{\rm pulse}_{ia}(t) \end{cases}, \quad (31)$$

where dots denote time derivatives. By defining the auxiliary quantities

$$q_{ia}(t) = \frac{2\Re \delta \rho_{ia}(t)}{\sqrt{2(f_i - f_a)}}, \quad p_{ia}(t) = -\frac{2\Im \delta \rho_{ia}(t)}{\sqrt{2(f_i - f_a)}}, \quad (32)$$

$$K_{ia,jb} = \sqrt{2(f_i - f_a)} K^{\rm Hxc}_{ia,jb} \sqrt{2(f_j - f_b)}, \quad \text{and} \quad v_{ia}(t) = \sqrt{2(f_i - f_a)} v^{\rm pulse}_{ia}(t), \quad (33)$$

Eq. (31) can be written in convenient form as

$$\begin{cases} \dot{q}_{ia}(t) = \omega_{ia} p_{ia}(t) \\ \dot{p}_{ia}(t) = -\omega_{ia} q_{ia}(t) - \sum_{jb} K_{ia,jb} q_{jb}(t) - v_{ia}(t) \end{cases}. \quad (34)$$

These equations are identical to the equations of motion of a collection of coupled classical harmonic oscillators when $q_{ia}(t)$ and $p_{ia}(t)$ are identified as position and momentum coordinates. In this notation, the electron-hole decomposition of energy of Eq. (29) is

$$E_{ia}(t) = \frac{1}{2} \left[\omega_{ia} p^2_{ia}(t) + \omega_{ia} q^2_{ia}(t) + q_{ia}(t) \sum_{jb} K_{ia,jb} q_{jb}(t) \right], \quad (35)$$

and the Coulomb energy contribution from Eq. (29) is

$$E^{\mathrm{C}}_{ia}(t) = \frac{1}{2} q_{ia}(t) \sum_{jb} K_{ia,jb} q_{jb}(t). \tag{36}$$

Supplementary Note S3: Rate of energy change.

By evaluating the time differential of Eq. (35) and using the equations of motion of Eq. (34), the rate of change of the electronic energy is obtained as

$$\dot{E}_{ia}(t) = \underbrace{\frac{1}{2}\left[q_{ia}(t) \sum_{jb} K_{ia,jb} \dot{q}_{jb}(t) - \dot{q}_{ia}(t) \sum_{jb} K_{ia,jb} q_{jb}(t) \right]}_{\text{interaction}} \underbrace{-v_{ia}(t)\dot{q}_{ia}(t)}_{\text{photoabsorption}}, \tag{37}$$

where the terms related to the interaction between electron-hole transitions and to photoabsorption have been identified. When summing over all transitions, the interaction term vanishes due to the symmetry of the $K_{ia,jb}$ matrix (see note above), and the total rate of change is

$$\Delta\dot{E}(t) = \sum_{ia} \dot{E}_{ia}(t) = -\sum_{ia} \dot{q}_{ia}(t) v_{ia}(t) = -\sum_{ia}^{f_i > f_a} 2\Re\delta\dot{\rho}_{ia}(t) v^{\mathrm{pulse}}_{ia}(t) = \delta\dot{\mu}(t)\mathcal{E}(t), \tag{38}$$

where $\delta\mu(t)$ is the induced dipole moment.

Supplementary Note S4: Practical evaluation of energy and its rate of change.

In practical calculations, $E_{ia}(t)$, $E^{\mathrm{C}}_{ia}(t)$, and $\dot{E}_{ia}(t)$ can be evaluated without explicit knowledge of the $K_{ia,jb}$ matrix. This is done by employing Eq. (34), resulting in the following practical forms of Eqs. (35), (36), and (37):

$$E_{ia}(t) = \frac{1}{2}\Big[p_{ia}(t)\dot{q}_{ia}(t) - q_{ia}(t)\dot{p}_{ia}(t) - v_{ia}(t) q_{ia}(t) \Big], \tag{39}$$

$$E^{\mathrm{C}}_{ia}(t) = -\frac{1}{2}\Big[\omega_{ia} q^2_{ia}(t) + q_{ia}(t)\dot{p}_{ia}(t) + v_{ia}(t) q_{ia}(t) \Big], \tag{40}$$

and

$$\dot{E}_{ia}(t) = \underbrace{\frac{1}{2}\Big[p_{ia}(t)\ddot{q}_{ia}(t) - q_{ia}(t)\ddot{p}_{ia}(t) + v_{ia}(t)\dot{q}_{ia}(t) - \dot{v}_{ia}(t) q_{ia}(t) \Big]}_{\text{interaction}} \underbrace{-v_{ia}(t)\dot{q}_{ia}(t)}_{\text{photoabsorption}}, \tag{41}$$

respectively.

Supplementary References

[1] Casida, M. E. Time-Dependent Density Functional Response Theory for Molecules. In *Recent Advances in Density Functional Methods, Part I*; Chong, D. P., Ed.; World Scientific: Singapore, 1995; p 155.